



Earth surface reflectance climatology from 3 years of OMI data

Q. L. Kleipool,¹ M. R. Dobber,¹ J. F. de Haan,¹ and P. F. Levelt¹

Received 18 April 2008; revised 20 June 2008; accepted 1 July 2008; published 24 September 2008.

[1] Global maps of the Earth's surface Lambertian equivalent reflectance (LER) are constructed using 3 years of Ozone Monitoring Instrument (OMI) measurements obtained between October 2004 and October 2007 at 23 wavelengths between 328 and 500 nm. The maps are constructed on a 0.5° by 0.5° longitude-latitude grid for each calendar month using an algorithm based on temporal histograms of the observed LER values per geophysical location. The algorithm allows seasonal effects related to vegetation, snow, and ice but excludes statistical outliers. The maps show typical features like open ocean regions with high reflectivity indicative of low phytoplankton levels, coastal waters with high reflectance caused by silt, and oceanic regions with low reflectance correlated with chlorophyll. Open oceans in general have a higher reflectivity than does land up to 420 nm. The highest reflectivity values of oceans occur at 380 nm. Good agreement is found with a similar LER map based on data from the Total Ozone Mapping Spectrometer (TOMS) at 331, 340, 360, and 380 nm, which is 0.015 lower on average. The comparison with data from the Global Ozone Monitoring Experiment (GOME) at 335, 380, 440, and 494 nm is also satisfactory, being 0.005 lower on average. The LER derived from OMI data is approximately 0.02 higher than the black sky albedo as derived from the Moderate Resolution Imaging Spectroradiometer at 470 nm, which is partly related to viewing geometry effects of the bidirectional reflectance distribution function of the surface. The data set presented contains residual cloud features over tropical rain forest regions, has a higher spatial resolution than those created using TOMS and GOME data, and includes more wavelengths.

Citation: Kleipool, Q. L., M. R. Dobber, J. F. de Haan, and P. F. Levelt (2008), Earth surface reflectance climatology from 3 years of OMI data, *J. Geophys. Res.*, 113, D18308, doi:10.1029/2008JD010290.

1. Introduction

[2] Retrieval of trace gases and cloud and aerosol properties in the Earth's atmosphere requires an accurate determination of the surface reflectance, especially when tropospheric trace gas column densities are desired. Studies of the accuracy of NO_2 total columns from Global Ozone Monitoring Experiment (GOME) by *Martin et al.* [2002] show that the error in NO_2 columns over major continental source regions is dominated by errors in the air mass factor caused by inaccurate estimates of the surface reflectances. This is confirmed by *Boersma et al.* [2004], who show that, under heavily polluted conditions, an absolute error of 0.01 in the surface reflectance induced a 15% error in the derived tropospheric NO_2 column. *Veeffkind et al.* [2000] show that an error of 0.01 in surface reflectance yields an aerosol optical thickness retrieval error of 0.1 in the ultraviolet. According to *Koelemeijer et al.* [2001], an error in the surface reflectance of 0.02 induces errors up to 150 hPa in cloud top pressures from GOME oxygen A-band measurements, depending strongly on the cloud fraction and the

surface reflectance itself. These examples show the importance of having an accurate surface reflectance map for retrievals of atmospheric properties in general.

[3] The reflectance of a surface, in the absence of polarization, is described by the bidirectional reflectance distribution function (BRDF) which is a function of the viewing geometry, illumination geometry and wavelength. By directional integration of the BRDF a quantity known as the spherical albedo can be derived which is defined as the ratio of upwelling to downwelling radiative flux. When the downwelling flux has no diffuse component this ratio is referred to as the "black sky" albedo or "directional-hemispherical reflectance" and is a function of solar zenith angle. When no directional component is present in the downwelling flux and when the diffuse component is isotropic the ratio is known as the "white sky" albedo. Current global albedo data sets have been derived from broadband sensors like the Advanced Very High Resolution Radiometer (AVHRR) [see *Csiszar and Gutman*, 1999], Moderate Resolution Imaging Spectroradiometer (MODIS) on EOS-Terra and EOS-Aqua [see *Schaaf et al.*, 2002; A. H. Strahler and J.-P. Muller, MODIS BRDF, albedo product, ATBD version 5, 1999], and the Multiangle Imaging Spectroradiometer (MISR) on EOS-Terra [see *Diner et al.*, 2002].

¹Royal Netherlands Meteorological Institute, De Bilt, Netherlands.

[4] The BRDF is sometimes directly used, for example, for the retrieval of aerosol properties from MODIS visible and near-infrared wavelengths [see *Levy et al.*, 2007]. However, the spherical albedo is not used in trace gases retrievals of solar backscatter instruments like Ozone Monitoring Instrument (OMI), Scanning Imaging Absorption Spectrometer for Atmospheric Cartography (SCIAMACHY), and GOME, because it is an integral over the full hemisphere. The BRDF is the appropriate quantity to describe the surface reflectance, but is unfortunately not well known at the shorter UV and VIS wavelengths. Therefore, most satellite retrieval methods of atmospheric composition use a different measure of the surface reflectance of the ground pixel that must satisfy a number of conditions. First, the angular dependency of the reflectance is explicitly dropped by assuming an isotropic reflecting surface known as an Lambertian surface. Second, the measure must be representative for the average viewing and illumination conditions the instrument encounters. Most instruments use either a scan mirror or two-dimensional detector to sample the surface of the Earth in the cross flight track direction; the width of the swath restricts the encountered viewing angles to a much narrower section of the hemisphere. In addition, instruments like OMI and GOME are in Sun-synchronous orbits and therefore always observe a ground pixel at the same local solar time, thus restricting the range of solar illumination angles.

[5] The Lambertian equivalent reflectance (LER) satisfies the aforementioned requirements; it is defined as the required reflectance of an isotropic surface needed to match the observed top of the atmosphere (TOA) reflectance in a pure Rayleigh scattering atmosphere under cloud-free conditions and no aerosols. The derivation of a surface reflectance data set is always severely hampered by clouds; approximately 60–75% of the Earth is instantaneously covered by clouds [see *Le Treut et al.*, 2007; *Wylie et al.*, 2005], depending whether thin clouds are included. For satellite observation this leads to the fact that only 20% and 10% of all pixels have a cloud fraction smaller than 5% for ground pixel dimensions of 10 by 10 km and 100 by 100 km, respectively [see *Krijger et al.*, 2007]. Smaller ground pixel dimension do increase the chance of a cloud-free pixel but the natural lower limit remains at 25–40%. In order to derive the surface reflectance it would be advantageous to remove all clouded measurements. Unfortunately it is not possible to use cloud data from the OMI instrument itself to screen the measurements, because the cloud retrieval algorithms strongly rely on the surface reflectance data set. For this reason, cloud contamination in a LER climatology can only be reduced by using large amounts of measurements and some statistical method.

[6] Currently, two LER data sets have been constructed using the space-borne spectrometers Total Ozone Mapping Spectrometer (TOMS) on Nimbus 7 [*Herman and Celarier*, 1997] (hereinafter referred to as HC97) and GOME on ERS-2 [*Koелеmeijer et al.*, 2003] (hereinafter referred to as KHS03). The TOMS instrument measures at 313, 318, 331, 340, 360 and 380 nm. The HC97 set is based on 14.5 years of data measured between November 1978 and May 1993 and has a spatial resolution of 1.0° by 1.25° . The wavelengths used in the HC97 data set are 331, 340, 360 and 380 nm. The KHS03 data set is based on 5.5 years of data

measured between June 1995 and December 2000 and has a spatial resolution of 1.0° by 1.0° . The GOME instrument measures between 237 and 794 nm with a 0.2–0.4 nm resolution. The 11 wavelengths used in the KHS03 data set are 335, 380, 416, 440, 463, 494, 555, 610, 670, 758, and 772 nm. The OMI instrument on board NASA's EOS-Aura satellite is a hyper spectral imager in the 270–500 nm wavelength range, launched on 15 July 2004. Two aspects of the OMI instrument make it very suitable for the derivation of a LER climatology. The smaller ground pixels (compared with other UV satellite sensors) in combination with OMI's ability of nearly global coverage in one day results in good statistics for each ground pixel, thus allowing to derive a data set with a 0.5° by 0.5° spatial resolution, using only 3 years of data obtained between October 2004 and October 2007, at 23 wavelength bands. The general approach is to build histograms of the various LER values that are observed in time over a certain ground scene. Cloudy observations will then populate the higher part of the histogram while the lower parts of the histograms are due to cloud-free conditions. Using a statistical algorithm the ground scene's LER is onward determined from the histogram.

[7] The objective is to derive a LER data set from OMI data to support and improve the retrievals of atmospheric constituents from OMI measurement data and from similar instruments. The objective is not to derive a full angular dependent data set like the BRDF; for this other instruments are more suitable. Using a LER climatology based on OMI data for retrievals of atmospheric constituents from OMI data has the advantage that it includes all wavelengths specific to OMI level 2 retrievals, thus reducing the errors from interpolation required by other LER sets. In addition, errors in the OMI retrievals, from unaddressed instrumental effects and natural surface reflectance long-term trends, will be reduced because the OMI LER climatology is based on the same data used in level 2 retrievals. Retrievals of atmospheric properties from data of other instruments may benefit from the higher spatial resolution of the OMI LER climatology. The OMI data set can be considered to be an extension and continuation of HC97 and KHS03, with a higher spatial resolution, additional wavelengths in the ultraviolet/visible wavelength range and recent temporal information.

[8] The paper is structured as follows. Section 2 describes the formalism used to derive surface reflectance in general. Section 3 describes the OMI instrument and its performance. Section 4 describes the data used and the various steps taken to obtain global surface reflectances, including seasonal- and wavelength-dependent effects. Section 5 gives an overview of all uncertainties involved in the process and an estimate of the overall error in the data set. Section 6 compares the data set to other data sets. Section 7 shows typical results obtained with the OMI mission LER. Section 8 gives some concluding remarks and an outlook for future work.

2. Methodology

2.1. Lambertian Equivalent Surface Reflectance

[9] The general approach in deriving the Lambertian equivalent surface reflectance is to calculate the narrow

band top of the atmosphere (TOA) reflectance for the specific wavelength of interest. These data are then corrected for a Rayleigh scattering atmosphere above an (unknown) Lambertian surface, assuming cloud-free conditions and no aerosols, such that the observed and modeled TOA reflectivity are equal. The resulting Lambertian equivalent reflectance can onward be mapped on a rectangular latitude-longitude grid. The data are grouped over certain time periods to yield distribution functions (histograms) of the observed LER per grid box. These histograms, measured at multiple viewing and illumination angles, contain all data measured over each grid box, and thus include effects due to cloud features, atmospheric variations in ground haze, absorbing aerosols, and precipitation. Interpretation of these histograms allows for the derivation of the most probable or the most likely surface reflectance that is needed in retrieval algorithms of level 2 data products. This method will only work if sufficient measurement data are available, which is the case for OMI already after 3 years due to the small ground pixels and large swath width.

[10] The reflectance R at the top of the atmosphere is defined by

$$R = \frac{\pi I}{\mu_0 E_0}, \quad (1)$$

in which I is the radiance reflected by the Earth (in $\text{Wm}^{-2}\text{nm}^{-1}\text{sr}^{-1}$), E_0 is the incident solar irradiance at the top of the atmosphere perpendicular to the solar beam (in $\text{Wm}^{-2}\text{nm}^{-1}$), and μ_0 is the cosine of the solar zenith angle θ_0 on the ground. Assuming a Lambertian isotropic surface reflectivity A_s , the TOA reflectance R can be expressed as

$$R(\mu, \mu_0, \phi - \phi_0) = R_0(\mu, \mu_0, \phi - \phi_0) + \frac{A_s t(\mu_0) t(\mu)}{1 - A_s s^*}, \quad (2)$$

in which μ is the cosine of the viewing zenith angle θ on the ground [see *van de Hulst*, 1980]. The first term in equation (2), R_0 , describes the atmospheric reflectance in the absence of a surface. The second term describes the reflectance caused by the surface, including multiple reflections between atmosphere and surface. The function t describes the total atmospheric transmission (including forward scattering), and s^* is the spherical albedo of the atmosphere for illumination from below. The Lambertian equivalent reflectance of the surface A_s needed to match the observed TOA reflectance can be written as

$$A_s = \frac{R - R_0}{t(\mu) t(\mu_0) + s^*(R - R_0)}. \quad (3)$$

This Lambertian approximation is more valid at the shorter wavelengths because the surface flux is largely diffuse in the UV owing to high Rayleigh optical depth. This results in weak anisotropy at the shorter wavelengths, while in the visible many surfaces are strongly anisotropic owing to the dominant direct beam illumination in combination with surface structure and shadowing effects.

2.2. Atmospheric Correction

[11] All atmospheric parameters as given in equation (2) must be calculated using a radiative transfer model. How-

ever, it is not computationally feasible to use a radiative transfer model to perform the calculation for every single OMI measurement. Therefore, a lookup table has been created using a polarized atmospheric radiative transfer model that contains the atmospheric reflection and transmission properties for all wavelengths, geometries, surface elevations, and total ozone columns that may prevail. For a purely Rayleigh scattering atmosphere, the dependence of R_0 , as given in equation (2), on the azimuth difference between the satellite and the Sun, $\phi - \phi_0$, can be written as

$$R_0(\mu, \mu_0, \phi - \phi_0) = \sum_{m=0}^2 a_m(\mu, \mu_0) \cos m(\phi - \phi_0), \quad (4)$$

which allows for a size reduction of the table [see *Koelemeijer et al.*, 2003]. The lookup table describes the coefficients $a_m(\mu, \mu_0)$, the total atmospheric transmission $t(\mu)$ and the spherical albedo of the atmosphere from below s^* as a function of surface pressure P , ozone column density Ω and wavelength λ . By interpolation in this lookup table and using equation (4), the atmospheric reflectance can be found as a function of μ , μ_0 , $\phi - \phi_0$, P_s , A_s and Ω for each value of λ . The lookup table has been created using a polarized plane-parallel radiative transfer model which uses a doubling-adding scheme by *De Haan et al.* [1987] and *Stammes* [2001], referred to as the doubling-adding-KNMI (DAK) model. The table gives the three Fourier terms for values of μ and μ_0 , ranging from 0 to 1 with equidistant steps of 0.01, total ozone columns ranging from 100 to 600 Dobson Units (DU) in steps of 50 DU and surface pressure (ground elevations) ranging from 0 to 10 km in steps of 2 km. Atmospheric data are based on an AFGL midlatitude summer profile, and the ozone absorption cross sections are taken from the works of *Brion et al.* [1993, 1998], *Daumont et al.* [1992], and *Malicet et al.* [1995]. These cross sections are convolved with a flat-topped Gaussian spectral slit function which best describes the OMI spectral response [*Dirksen et al.*, 2006] in order to obtain the desired 1.4 nm wide resolution of the band averaged OMI TOA reflectivity.

3. The OMI Instrument

3.1. Instrument Description

[12] The Ozone Monitoring Instrument onboard the NASA EOS-Aura satellite is a hyper spectral passive imager in the 270–500 nm wavelength range employing two-dimensional detector arrays. One dimension is used to measure the spectral information while the second is used to instantaneously sample all cross-track ground pixels. The wavelength range is covered by three optical channels, namely UV1 (264–311 nm), UV2 (307–383 nm) and VIS (349–504 nm). The satellite was launched on 15 July 2004 into a Sun-synchronous orbit at 705 km altitude with an ascending node equator crossing time of 1345. An overview of the Aura mission is given by *Schoeberl et al.* [2006]; the OMI experiment and its science objectives are described by *Levelt et al.* [2006a, 2006b]. Detailed information concerning the instrument is given by *Dobber et al.* [2008a]; the data processing is described by *Oord et al.* [2006] and the main data products are described by *Veeffkind et al.* [2006], *Bucsela et al.* [2006], *Krotkov et al.* [2006],

Table 1. Wavelength Bands for the Surface Reflectance

Wavelength	Source ^a	Purpose
309.3	UV2	calibration ^b
312.0	UV2	calibration ^b
320.0	UV2	delta ozone correction ^b
328.1	UV2	ozone ^c
335.0	UV2	ozone ^d
342.5	UV2	aerosol ^c
345.4	VIS	LER
354.0	VIS	aerosol ^c
367.0	VIS	aerosol ^c
372.8	VIS	LER ^c
376.5	VIS	calibration ^c
380.0	VIS	calibration ^{c,d,e}
388.0	VIS	aerosol
406.0	VIS	aerosol
416.0	VIS	aerosol ^d
418.2	VIS	LER
425.5	VIS	aerosol
440.0	VIS	NO ₂ ^d
442.0	VIS	aerosol
452.0	VIS	aerosol
463.0	VIS	O ₂ -O ₂ , aerosol ^d
471.0	VIS	MODIS, aerosol
477.5	VIS	O ₂ -O ₂ , aerosol
488.0	VIS	aerosol
494.5	VIS	O ₂ -O ₂ ^d
499.3	VIS	LER

^aUV1, 264–311 nm; UV2, 307–383 nm; VIS, 349–504 nm.

^bWavelengths that have been calculated but are not in the product.

^cWavelengths that are also in the HC97.

^dWavelengths that are also in KHS03.

^eWavelength is also measured in the UV2 channel.

Tanskanen *et al.* [2006], Joiner and Vasilkov [2006], and Loppelmeier *et al.* [2006].

[13] The combination of a two-dimensional detector array and the wide field of view of 115° allows OMI to measure backscattered radiance with global coverage on a daily basis with a 13 km by 24 km resolution in the nadir position. Once per day the solar irradiance is measured through the solar port for about two minutes over an onboard quartz volume reflection diffuser. Top of the atmosphere (TOA) reflectance data are not an official OMI data product, but can be obtained as the ratio of the Earth radiance over the solar irradiance (both of which are official level 1B data products). TOA reflectance is used to derive total column amounts of ozone, NO₂ and some other minor species. Aerosol, cloud information and ozone vertical profiles are also derived as standard products from OMI measurement data.

3.2. Instrument Performance

[14] The accuracy of the TOA reflectance is solely determined by instrument performance. A complete description of the OMI instrumental calibration and performance is given by Dobber *et al.* [2006, 2008a]. Because most of the optical components of the instrument, as well as most detector properties, are common to the radiance and irradiance optical paths, the sensitivity of these will cancel out in the ratio of Earth over Sun measurements. The ratio of the radiance over irradiance absolute radiometric calibration is known as the instrument bidirectional scattering distribution function (BSDF), which includes the onboard quartz diffuser. Because of the aforementioned reason, this BSDF can be determined to a higher accuracy than the individual

radiance and irradiance response functions. On-ground calibration of the BSDF yielded absolute accuracies of 1% (1 σ) for nadir and 1.5–4% (1 σ) when all viewing directions are taken into account, as discussed by Dobber *et al.* [2006]. These values are confirmed with in flight data by Jaross and Warner [2008] and Dobber *et al.* [2008a]. The calibrated solar spectrum, as measured by OMI, has been compared to various high- and low-resolution solar reference spectra by Dobber *et al.* [2008b]; in this study absolute agreement has been found to be better than 4% (1 σ). Moreover, in-flight calibration of the swath dependence of the absolute irradiance has been improved to 0.2% for the UV2 and VIS channels for collection 3 data as discussed by Dobber *et al.* [2008a]. Typical signal-to-noise ratios (SNR) of a daily irradiance range between 1000 and 4000, while the typical SNR of a single radiance measurement is approximately 800. The systematic error in the TOA reflectance is dominated by the uncertainty in the BSDF, yielding 1% for the nadir position and 1.5–4% for the extreme cross-track positions.

3.3. Instrument Degradation

[15] The optical degradation of the instrument after 3 years of service is less than 1% for both the radiance and irradiance mode as discussed by Dobber *et al.* [2008a]. The degradation of the detectors mainly results in increased dark current but this is accurately corrected for by the ground data segment processor [see Dobber *et al.*, 2006]. Both these degradations have no impact on the LER analysis as discussed in the remainder of this paper.

4. Derivation of the Global Surface LER From OMI Data

4.1. TOA Reflectance

[16] Results presented in this paper are based on OMI data taken from L1b collection 3 [see Dobber *et al.*, 2008a] over the epoch October 2004 to October 2007, comprising approximately 1.5 billion spectra. For each of the 26 wavelengths defined in Table 1, the averaged TOA reflectivity has been calculated for each cross-track position and all along-track positions for all available L1b files. Note that the first three wavelengths are not included in the LER climatology product owing to their large uncertainty.

[17] The number of pixels averaged over in the wavelength dimension is not equal for each OMI optical channel owing to the different spectral resolutions. The number of wavelength pixels used are 7 and 5 for the UV2 and VIS channels, respectively. This yields an effective bandwidth of 1.4 nm when the spectral slit function is taken into account. In order to obtain the TOA reflectance, the measured Earth radiance has to be divided by the incoming solar irradiance. The irradiance as measured by OMI is a daily averaged level 1B product obtained from the OMI Trend Monitoring and in-flight Calibration Facility (TMCF) [see Oord *et al.*, 2006]. The wavelength scales differ between the radiance and irradiance for each individual measurement. These differences are partly due to inhomogeneous illumination of the entrance slit of the spectrometer as a result of nonuniform ground scenes [see Voors *et al.*, 2006]. The different scales may also result from temperature variations of the optical bench for the radiance data. Therefore, each

radiance spectrum is interpolated to the wavelength grid of the irradiance.

4.2. Surface Reflectance

[18] The Lambertian equivalent surface reflectivity is calculated using the lookup table and equations (3) and (4). The required ground elevation, solar zenith and azimuth angles, as well as the viewing zenith and azimuth angles are provided in the level-1b file. However, the required total ozone column is not known and has to be estimated. For this purpose an a priori value of the total ozone column is provided by an ozone map based on a 5-year climatology of assimilated GOME data taken from the Tropospheric Emission Monitoring Internet Service (publicly available at <http://www.temis.nl>). This a priori total ozone column is included in the lookup table and further improved by a first-order ozone retrieval using the TOA reflectance data: Assume we have derived approximate values for the surface albedo A_s at two wavelengths, A_1 and A_2 , while using the a priori ozone column N_a . To correct for the ozone difference ($N - N_a$) we use a Taylor series expansion for the derived surface albedo, omitting higher-order terms:

$$A_k = A + \frac{\partial A_k}{\partial N_a} (N - N_a), \quad (5)$$

where we explicitly assume that the surface albedo A does not depend on the wavelength and that all spectral variation in the retrieved albedo is due to an incorrect assumption of the total ozone column. Equation (5) provides us with two equations ($k = 1, 2$) for the two unknowns, A and $\Delta N = N - N_a$. Solving the equations for ΔN yields

$$\Delta N = (A_1 - A_2) / \left(\frac{\partial A_1}{\partial N_a} - \frac{\partial A_2}{\partial N_a} \right). \quad (6)$$

Using this equation the expression for the actual surface albedo becomes

$$A = A_1 - \frac{\partial A_1}{\partial N_a} \cdot \Delta N. \quad (7)$$

Hence, to calculate the actual albedo A , the partial derivatives are needed which can be obtained from equation (3) by noting that R is the measured reflectance which does not change when the a priori column changes. Note that this approach effectively forces the LER at two wavelengths to be equal. The LER value at a single wavelength has to be sacrificed in order to improve the LER at all other wavelengths. The wavelength pair that yielded the best match with the official ozone product is the combination of 320 and 342 nm. Since the 320 nm and the 342 nm reflectance values are equal the 320 nm value is omitted from the surface reflectance product. The values below 320 nm are also omitted from the final product because the strong ozone absorption obscures the ground signal and thus renders the derived values unreliable. Therefore, the lowest reliable wavelength in the climatology is 328 nm.

4.3. Global LER Maps

[19] The derived LER is mapped on a rectangular latitude-longitude grid with an resolution of 0.5° by 0.5° . These maps

are created for each month, and include data from all corresponding months over the period under investigation, for example, all data from January 2005, 2006 and 2007 are combined in a single map, which leads to 90 d of full global coverage data to be included in each map. For each grid box the map holds a distribution function (histogram) of the observed LER values ranging from 0.00 to 1.10 with steps of 0.01. Because of the equal angular extent of each OMI ground pixel in combination with the varying distance between the satellite and the viewing point on Earth, not all ground pixels are of equal size in the cross-track direction. This means that depending on the viewing angle, a single measurement can completely fall within a single grid box or actually overlap several adjacent grid boxes. We take each measurement to be representative for the center location of the target grid box, that is, each measurement can only contribute to a single histogram. The first and last ground pixel of each cross-track measurement, which correspond with the most extreme viewing angles, are not included in the histograms because they have the largest ground pixel size; the largest pixels taken into account are 120 km by 13 km at the equator. Data measured at solar zenith angles greater than 70° are not included in the histograms because the lookup table is only accurate for lower values (see section 5).

4.4. Interpretation of the Histograms

[20] The observed reflectances are due the underlying surface but may also contain cloud features and features due to snow and ice, which all tend to increase the reflectance. In the ultraviolet wavelength region the reflectance may be artificially lowered by absorbing aerosols. The latter effect is not present in the visible range; for this reason we have used the 494 nm band for the interpretation of the histograms (see section 4.5). The histograms contain all data measured over the grid box and from these the surface reflectance corresponding to the cloud-free case must be derived. Since clouds, snow and ice all tend to increase the reflectance it is common practice to take the absolute minimum observed reflectance to be representative for the surface. The lowest value present in a histogram constitutes the minimum Lambertian equivalent reflectance (MLER), which is the value as provided by KHC03. However, *Herman et al.* [2001] argue that this value may not be the most appropriate value for satellite retrievals of atmospheric composition and that instead the more frequently occurring scene reflectivity, caused by both surface and the presence of boundary layer haze and aerosol, should be used. Because of ground and cloud shading effects and darkening by precipitation, the MLER is very likely to underestimate the scene's overall reflectivity. In addition, the absolute minimum value of the histogram will correspond to the lowest value of the BRDF at a specific illumination and viewing angle. For all aforementioned reasons, the MLER is not a good measure of the most probable LER of a ground scene and a method has been developed to yield a better estimate of the surface reflectance. In order to obtain this LER, statistics for each ground pixel are calculated containing the mean, the mode (most frequently observed value), the standard deviation, the full width at half maximum (FWHM) and the absolute minimum and maximum of the histogram. In addition, the running integral of the

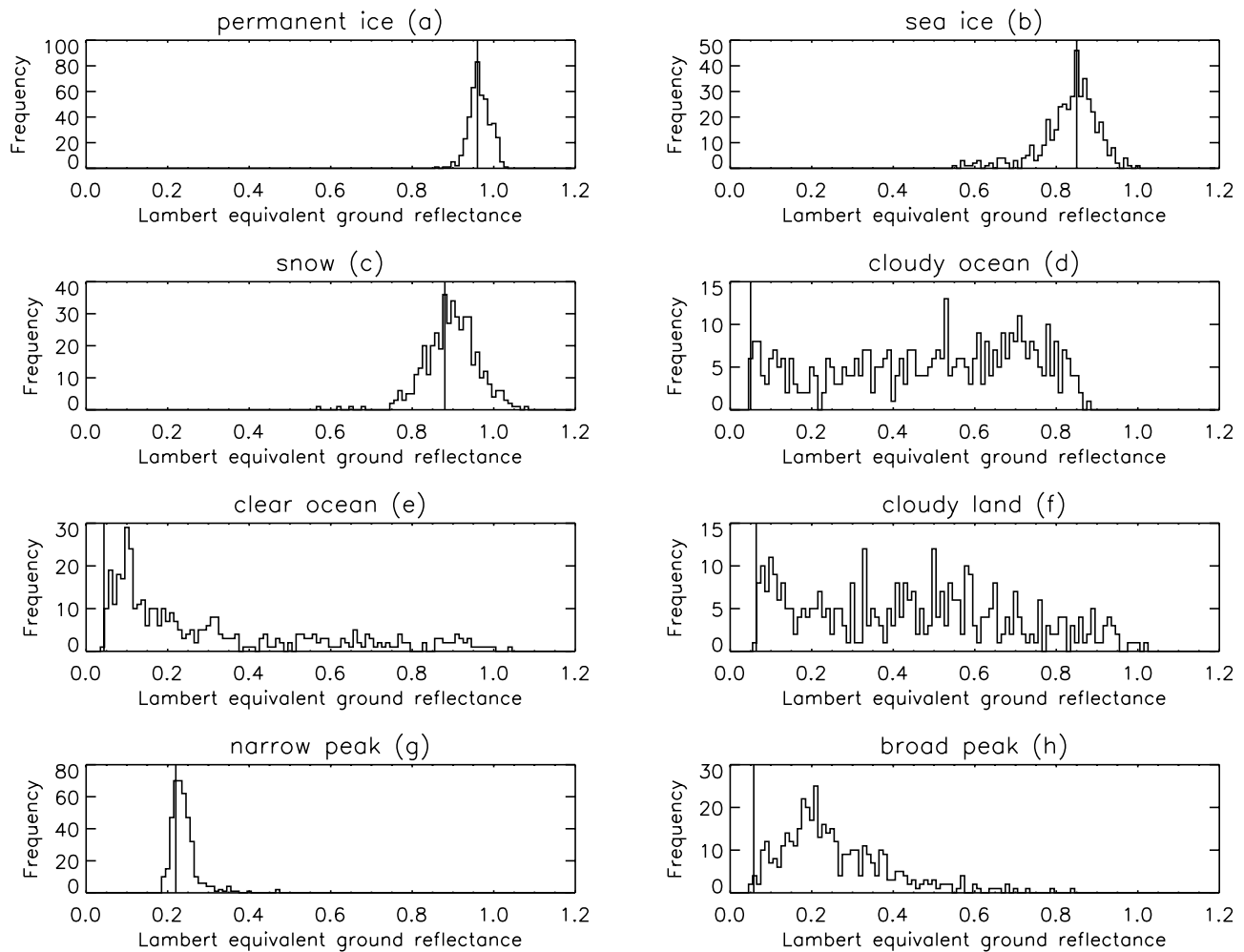


Figure 1. (a–h) Typical distribution functions for the various methods used to derive the Lambertian equivalent ground reflectance (LER). The histograms contain all data of the month January between 2004 and 2007. Each histogram contains approximately 400 individual measurements of the LER for a ground pixel of 0.5° by 0.5° . The derived surface reflectance is indicated with a solid line.

histogram, from lower to higher values, is calculated. This is also referred to as the cumulative probability function. In order to improve the interpretation of the histograms a digital elevation map containing land types is used, based on GTOPO30 data (publicly available through <http://edc.usgs.gov/>), and which is part of the SDP toolkit (see A. Taaheri, Release 7 SDP Toolkit Users Guide, 333-EMD-001, Revision 04, March 2006, Raytheon Co., available at <http://edhs1.gsfc.nasa.gov/waisdata/toc/333emd001r4toc.html> 2006). Daily nominal ice and snow extent data taken from NISE [see *Nolin et al.*, 1998] is used to distinguish between snow, ice and clouds. The interpretation of the distribution functions is based on a sequential algorithm which checks certain scenarios until a match is found in the following order:

[21] 1. If the histogram contains less than 50 measurements, it is not further analyzed, because the result is expected to be unreliable. In a later stage this pixel will be filled with a valid value, taken from the closest month.

[22] 2. If the NISE data indicate that the ground pixel was covered with permanent ice for more than 20% of the

measurements, the mode is taken as the surface reflectance (see Figure 1a).

[23] 3. If the NISE data indicate that the average sea ice concentration exceeds 1%, the mode of the histogram is taken to be the value of the surface reflectance (see Figure 1b).

[24] 4. If the NISE data indicate that 10% of the measurements were taken over snow, and the average LER exceeds 0.50, the mode of the histogram is taken as the surface reflectance (see Figure 1c).

[25] 5. We use the DEM map to determine whether a pixel is over water. If the pixel is over water, and if the FWHM of the histogram exceeds 0.20, the pixel is assumed to be cloudy, and the surface reflectance is taken to be the 1% cumulative probable value of the histogram (see Figure 1d).

[26] 6. All remaining areas over water are considered cloud free, and the surface reflectance is taken to be the 1% cumulative probable value of the histogram (see Figure 1e).

[27] 7. Cloudy pixels over land are found using the DEM map and the criterion that the FWHM of the histogram exceeds 0.20. The surface reflectance for these ground

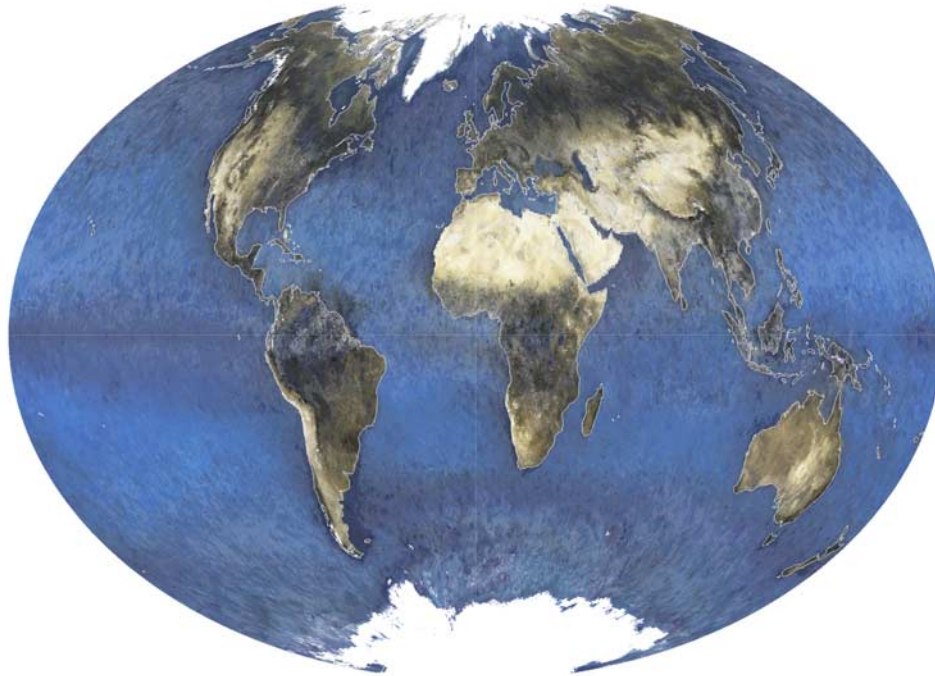


Figure 2. Composite color image based on the absolute mission minimum LER. Residual cloud structures are visible over the northern part of South America, Southeast Asia, China, and central Africa.

pixels is taken to be the 1% cumulative probability of the histogram (see Figure 1f).

[28] 8. Histograms with very narrow distinct peaks are typical for arid desert areas. For these pixels the FWHM is lower than 0.10, and the surface reflectance is taken to be the mode of the histogram (see Figure 1g).

[29] 9. Broader peaks over land (FWHM less than 0.20 but larger than 0.10) indicate less arid areas with more vegetation; for these areas the surface reflectance is taken to be the 1% cumulative probable value of the histogram (see Figure 1h).

[30] 10. The absolute minimum of the histogram is used for all ground pixels that have not been assigned surface reflectance value at this stage.

[31] 11. The last step is to correct all ground pixels that have been assigned a null value owing to some outliers. In this case the value is overwritten by the absolute minimum.

[32] The 1% cumulative probability threshold has been chosen to remove outliers due to shading effects and darkening by precipitation while retaining the lowest value. The thresholds and the above algorithm steps have been carefully optimized by inspecting a large number of histograms for all prevalent land types and seasons. The cumulative threshold is equal for all histograms even though they are classified differently (e.g., cloudy and noncloudy water). The terms “cloud free” and “cloudy” are based on the statistics of the histogram, and therefore not exclusive; there will always remain a portion of overlap and uncertainty. These description are mere indications of the amount of cloudiness of the ground pixel. The actual values chosen for the surface reflectance are the same in both cases (1% cumulative threshold). The classification “cloudy” or “non-

cloudy” is only used to guide the process of removing possible residual cloud contamination as described in section 4.7.

[33] Typical histograms for each type of classification are shown in Figure 1. The histograms shows that permanent ice, in general, has a higher reflectance than sea ice (Figures 1a and 1b), while snow (Figure 1c) has approximately the same distribution function as sea ice. Permanent ice also has a narrower distribution than sea ice or snow over land. Cloudy scenes over land (Figure 1f) and over sea (Figure 1d) both show a significant number of measurements with high reflectivity that cannot be attributed to the true surface reflectivity but must be attributed to clouds. Less cloudy ocean is typically more peaked and narrow. Broad peaked distributions as shown in Figure 1h are more difficult to interpret and are analyzed according to the above mentioned sequential algorithm. A typical example for arid, cloud-free ground scenes is given in Figure 1g: This ground pixel lies in the Libyan desert and has a high reflectivity; its distribution is highly peaked and narrow.

4.5. Spectral Surface Reflectance

[34] The aforementioned algorithm derives LER maps for each calendar month at a single wavelength. There are two methods to derive the LER at various wavelengths. The first is to use the algorithm for each wavelength individually, and then to combine these to a spectral map. The second is to use a single wavelength to derive the LER and consecutively gather all the corresponding spectral measurements; this method has the advantage that the consistency between all wavelengths is guaranteed, because the spectral dependence is taken from the same scene. We use the second

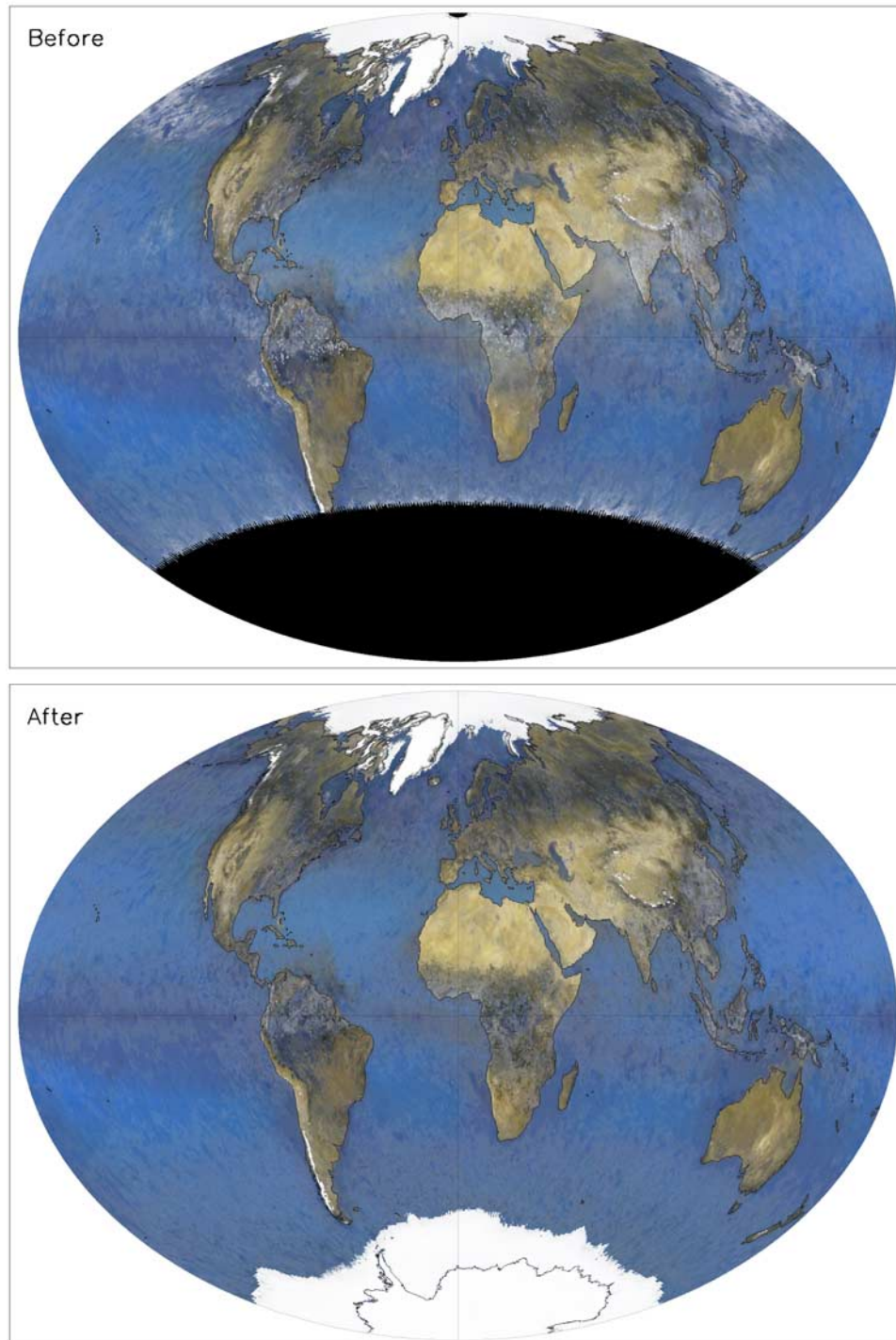


Figure 3. Composite color image showing the effect of the postprocessing steps. The top image shows the monthly map for July, before filling of missing pixels and before cloud replacement. The bottom image shows the same data set after cloud removal and filling of missing pixels.

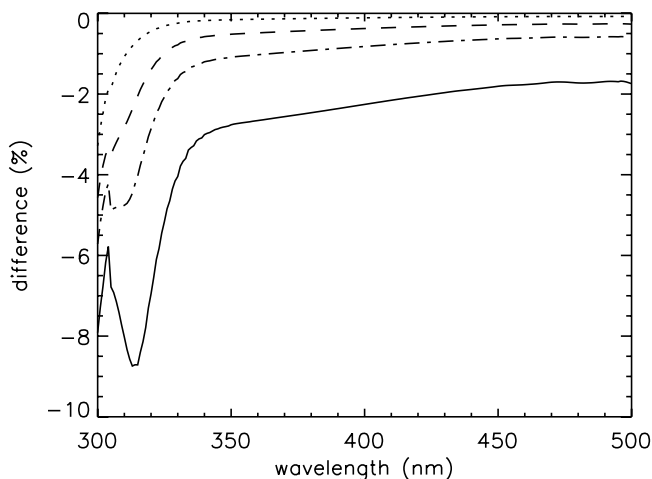


Figure 4. Fractional difference between a plane-parallel and a spherical radiative transfer model. The differences are given for a viewing angle difference of 0° and a surface albedo of 0.05 for an atmosphere containing air molecules and ozone. The viewing zenith angle is 0° , and the solar zenith angles are 60° (dotted line), 70° (dashed line), 75° (dash-dotted line), and 80° (solid line), respectively.

method and this is also the method used in the derivation of the KHS03 set. The approach was slightly modified to simultaneously obtain an estimate of the variability involved. The optimal wavelength to obtain the initial LER map for OMI is 494 nm. This is one of the highest wavelengths in the VIS channel and ensures good instrument performance and calibration. In addition, it is not sensitive to UV absorbing aerosols, thus making the climatology also usable for retrievals of aerosol information. Furthermore, the radiances and irradiances at this wavelength are not influenced by Solar Fraunhofer lines or absorption lines from atmospheric constituents. All the original measurements that were part of the histogram are examined again, and all spectra are collected for each ground pixel whose LER value at 494 nm matches the LER map within a threshold of 0.01 for that grid cell. After averaging these spectra, the ensuing product contains a consistent spectral database of LER values, together with an estimate of the variability.

4.6. Total Mission Map

[35] Once the spectral maps have been derived for all months, a minimum LER map is constructed for the total mission. The method is to combine the 12 monthly maps and take their absolute minimum LER value as the mission minimum LER. Ground pixels in the monthly maps that do not have sufficient points, that are out of range, or that have no corresponding histogram value, are explicitly excluded as input for the mission map. This causes some ground pixels in the mission map to have no value; these pixels are filled in from the closest grid box in the spatial direction. Most of these pixels are around the poles where the area of the pixels is very small.

[36] A composite color mission map, based on three wavelengths in the VIS channel, is shown in Figure 2. Because of seasonal effects and the 70° threshold on the

local solar zenith angle, the monthly maps have no data over the poles. These missing pixels are filled in with the values of the month nearest in time.

4.7. Residual Cloud Removal

[37] The ascending node overpass time of the Aura satellite is 1345 local time, and equatorial regions are nearly always cloudy at this time. For these regions cloud-free conditions are minimal and many ground pixels must be replaced, for example, over the tropical forests, Indonesia and India in the monsoon, and high latitudes in the winter periods. Therefore, all cloudy land and sea pixels in each monthly map are replaced with their cloud-free value of the nearest month. The cloudy pixels are actually detected by the histogram algorithm; that is, based on the statistics of the distribution, a specific method is chosen to derive the surface reflectance, but at the same time a flag is raised how the value was obtained (see section 4.4 and Figure 1). If the “cloudy” flag is raised, this does not necessarily mean that the derived value is wrong, but that it could be contaminated. Therefore these pixels are replaced with pixels that do not have that flag raised. Such a pixel is searched in the nearest month. Note that the actual value of the reflectance is not used in the replacement algorithm.

[38] The replacement algorithm is demonstrated in Figure 3 for the month of July. The top image shows the composite color map before filling the high latitudes and before cloud replacement. Cloud structures can be seen over rain forest areas of northern South America, equatorial Africa, Southeast Asia, and parts of China as well as over the northern parts of the Pacific Ocean. The bottom image in Figure 3 shows the map after filling of the missing pixels and after replacement of the cloudy pixels. The improvement is evident, but still residual cloud features can be seen over the rain forest areas.

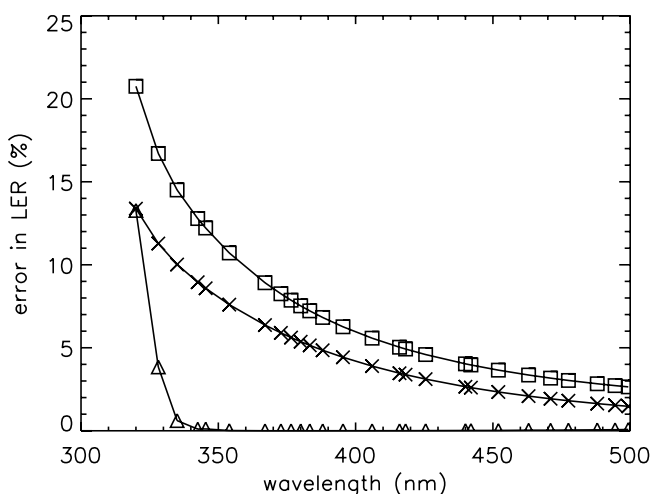


Figure 5. Error in LER caused by a 1% error in the top of the atmosphere (TOA) reflectivity (squares), a 10 hPa change in surface pressure (crosses), and a 1% error in the assumed total ozone column (triangles) as a function of wavelength. These data are for a true surface reflectivity of 0.05, solar zenith angle of 60° , nadir viewing, azimuth difference of 0° , true ozone column of 335 Dobson unit (DU), and a surface elevation of 0 km. The errors are given as a percentage of the true LER.

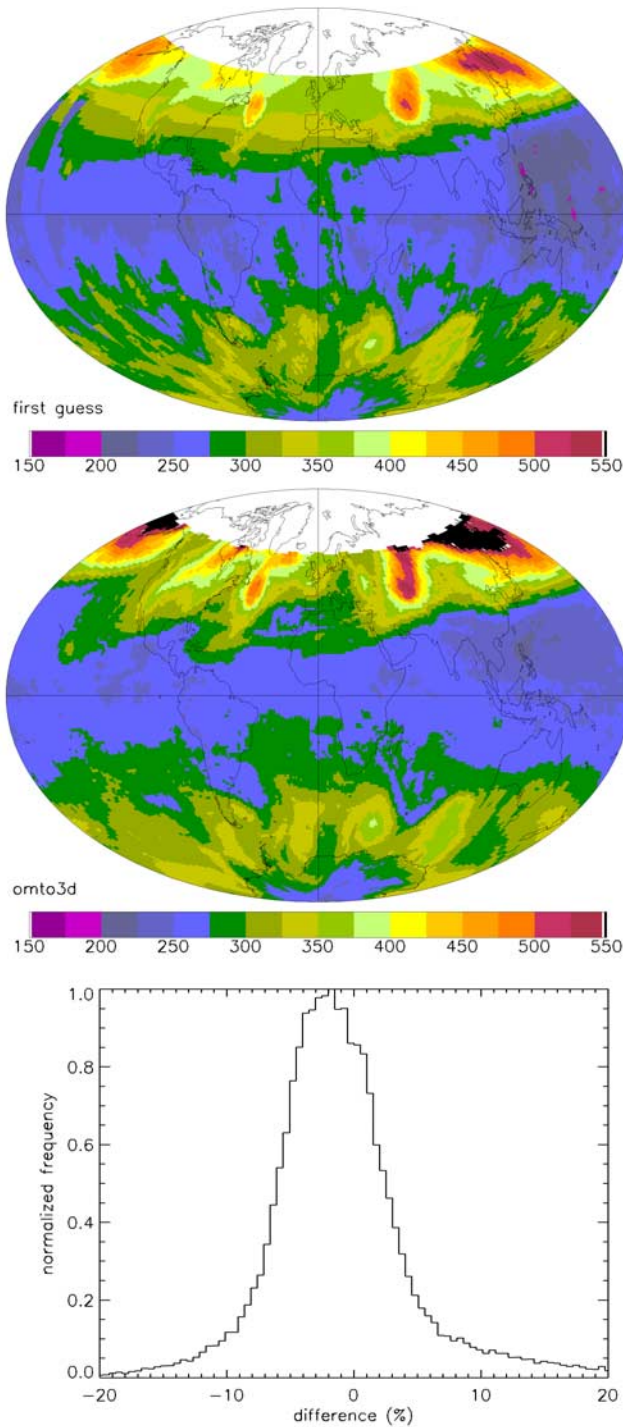


Figure 6. Accuracy of the (top) first-order ozone correction, compared to the (middle) regular level 3 gridded ozone product derived with the Total Ozone Mapping Spectrometer (TOMS) algorithm for 1 January 2007, both in DU. (bottom) The distribution of the fractional differences in percent.

[39] Forest scenes have surface reflectance values in the range of 0.04 to 0.06. In order to derive these values the cloud fraction must be very small. For example, assuming that the surface has a reflectivity of 0.05 and that the cloud

has a reflectivity of 0.80, then the observed scene reflectance will be 0.125 at a 10% cloud fraction. The chance of obtaining an image over the Brazilian Amazon with less than 10% cloud cover is as low as 40% on an annual basis as reported by *Asner* [2001], who studied cloud cover using Landsat data. The northern parts of the Amazon are even unattainable at the 10% level according to this study, even at the 30 m resolution of the Landsat imagers.

[40] The cloud contamination will reduce when more OMI data become available, but cloud contamination can never be completely avoided. Even though the derived LER values are too high to be caused by the underlying surface reflectance, they show that these clouds or ground mist patches are persistent and therefore could be considered to be an estimate of the scene's reflectance, representing a climatologically weighted average between ground and cloud reflectivity.

5. Error Analysis

5.1. Accuracy of the Atmospheric Correction

[41] The lookup table, used for the derivation of the surface reflectance climatology, has been generated with the same plane-parallel polarized atmospheric radiative transfer model that was used in the study by *Koелеmeijer et al.* [2003]. The use of a plane-parallel model will constrain the accuracy of the correction table at higher solar zenith angles because the curvature of the atmosphere cannot be ignored. A comparison has been made between the DAK model and a spherical model to quantify this effect. In Figure 4 the relative difference between the plane-parallel and spherical models is given for a surface albedo of 0.05 at various solar zenith angles. For wavelengths larger than 320 nm, the error in the reflectance due to the absence of a spherical approach is less than 1.5% for all solar zenith angles smaller than 70 degrees. No measurements with SZA larger than 70° are used in the construction of the histograms.

[42] In order to interpolate in the lookup table, accurate values are needed for the azimuth difference, the solar and viewing zenith angles, the surface elevation and the total ozone column. The solar and viewing angles are provided in the OMI radiance level 1b product and are therefore no source of additional errors. The surface elevation is also provided by the level 1b file. The surface pressure may, however, differ from the mid latitude atmospheric profile assumed in the lookup table. Figure 5 shows the effect of a 100 m uncertainty on the surface elevation. This roughly corresponds to a 10 hPa uncertainty on the surface pressure. For a midlatitude profile, the peak-peak climatologically swing in the pressure is approximately 40 hPa on 1000 mbar. The variation of the surface pressure introduces uncertainties in the derived surface reflectance of 15% at 320 nm, which reduces to 2% at 500 nm. The total ozone column is not known and can lead to errors in the calculated atmospheric reflectance. Figure 5 also shows the sensitivity of the predicted LER as a function of a 1% error in the estimation of the total ozone column Ω , for a true LER of 0.05. The error increases dramatically at shorter wavelengths as a result of the strong ozone absorption and can amount to 15% at 320 nm; above 342 nm the error is negligible. In order to improve the accuracy below 342 nm,

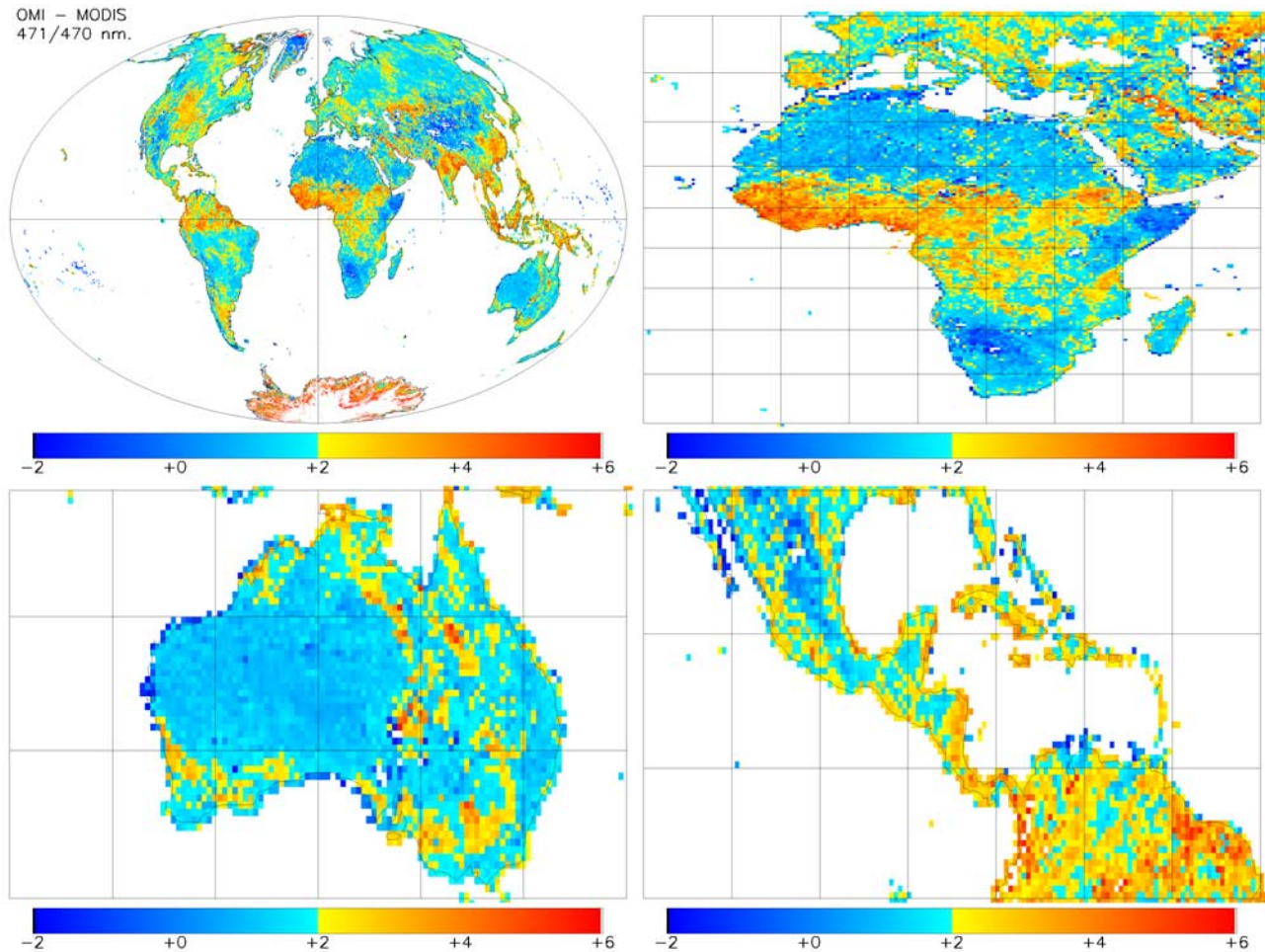


Figure 7. Comparison of Ozone Monitoring Instrument (OMI) LER data with Moderate Resolution Imaging Spectroradiometer (MODIS) black sky albedo at 470 nm. The MODIS channel is 20 nm wide. The values in the legend have been multiplied by 100.

a first-order ozone retrieval is performed during the calculation of the surface reflectance (see section 4.2) The accuracy of this algorithm has been verified by comparison of the total ozone column with the regular level 3 gridded OMI total ozone column product based on the TOMS algorithm. In Figure 6 both products are shown for a single day, as well as the distribution of the fractional differences. We find good overall agreement as most of the structures are reproduced. The mean difference amounts to -1.7% with a standard deviation of 11% ; the offset is partly caused by the fact that the first guess product is gridded using a minimum method thus yielding lower numbers. This will induce an error of -20% to $+24\%$ in the derived LER value at 328 nm , rapidly becoming negligible above 340 nm (see Figure 5). These errors are expected to average out in the calculation of the spectral LER because multiple observations of the same ground scene during a month will contain uncorrelated total ozone amounts.

5.2. Overall Accuracy

[43] The overall accuracy of the climatology can roughly be subdivided into two components. The first component is due to random and systematic instrumental errors propagating into the TOA reflectance. For a single TOA reflectance

measurement, the random error is dominated by the noise in the radiance which amounts to 800 SNR . The systematic errors are due to uncertainties in the overall instrument BSDF calibration which is estimated at 1% for the nadir position and up to 4% if all swath angles and wavelengths are taken into account. The sensitivity of the estimated LER as a function of wavelength to a 1% error in the assumed TOA reflectivity is given in Figure 5. Assuming an overall 2% error in TOA reflectivity, the error in LER amounts to 5% at 500 nm and 40% at 320 nm ; these values are relative percentages of the true LER. Another source of systematic errors is the optical degradation of the OMI instrument after 3 years in mission as discussed by *Dobber et al.* [2008a], which is below 1.0% for the UV and VIS channels.

[44] The second component of the overall error budget is caused by the interpretation of the histograms themselves. This error is difficult to quantify because the histograms contain LER values obtained at various viewing geometries; even though the Rayleigh correction removes the strongest atmospheric effects for all geometries, the true surface BRDF is still sampled at different viewing angles. This introduces an error in the case of land surface reflectance anisotropy (see A. H. Strahler and J.-P. Muller, MODIS BRDF, albedo product, ATBD version 5, 1999). Forward

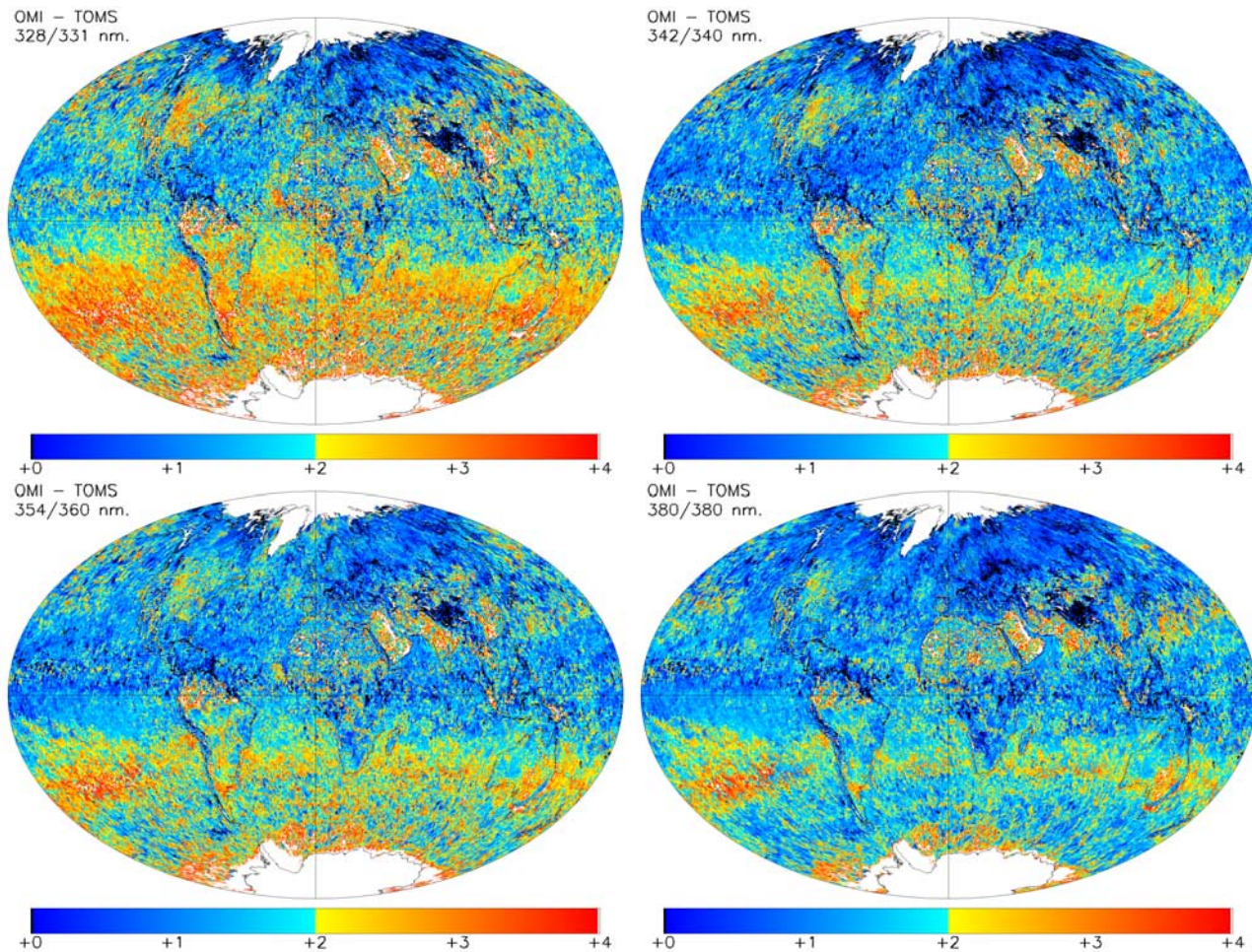


Figure 8. Difference in mission minimum LER between OMI and TOMS. The values in the legend have been multiplied by 100.

calculations for the reflectivity of a mixed scene over Europe based on MODIS BRDF parameters [Moody *et al.*, 2005], for representative OMI viewing angles, showed that the true angular reflectivity varied between 0.04 and 0.08. If the surface reflectance is taken to be the absolute minimum of each histogram, this will automatically sample the lowest value in the BRDF which is not a representative value for the overall LER of the ground pixel. In most cases the proposed method selects the 1% cumulative probable LER value as the surface reflectance; the validity of this choice has to be confirmed with results from level 2 trace gas data and atmospheric properties of clouds and aerosols. However, a full validation of these products and a more detailed investigation of illumination and viewing angle dependencies of the LER is beyond the scope of this paper, and is left for future work. The above uncertainty contributions lead to overall absolute uncertainties in the LER of 0.01–0.02 for the longer wavelengths and increasing values toward the shorter UV wavelength region.

6. OMI Comparison With Other Data Sets

6.1. Comparison With MODIS

[45] Comparison of the OMI data set with MODIS data is not straightforward because MODIS derives the anisotropy

of land surface reflectance using observations at multiple angles. The MODIS black and white sky albedos cannot be compared directly to OMI LER values for the following reasons: (1) albedo is the integral value over the full hemisphere which does not correspond to the range of solar zenith and viewing angles that OMI encounters, (2) the black sky albedo is valid for local solar noon which does not match the 1345 ascending node equator crossing time of OMI, and (3) the ratio between diffuse and direct illumination needed to obtain the true sky albedo can only be estimated because it depends on aerosol content and various other atmospheric properties. We calculated this illumination ratio with a radiative transfer model for several wavelengths, assuming a mid latitude summer profile in a atmosphere only containing air molecules and ozone, and no clouds or aerosols. The direct component at 440 nm is approximately 0.88 indicating that the OMI LER data are closest to the black sky albedo. The MODIS data set used for this comparison is the 5-year aggregation of MOD43B3 data derived by Moody *et al.* [2005] at 470 nm. All available 16-d black sky data sets were first resampled to match the OMI resolution by calculating the mean of all MODIS pixels that fall within an OMI pixel. We compare the minimum of these 16-d periods to the absolute minimum mission map from OMI. Figure 7 shows the difference at

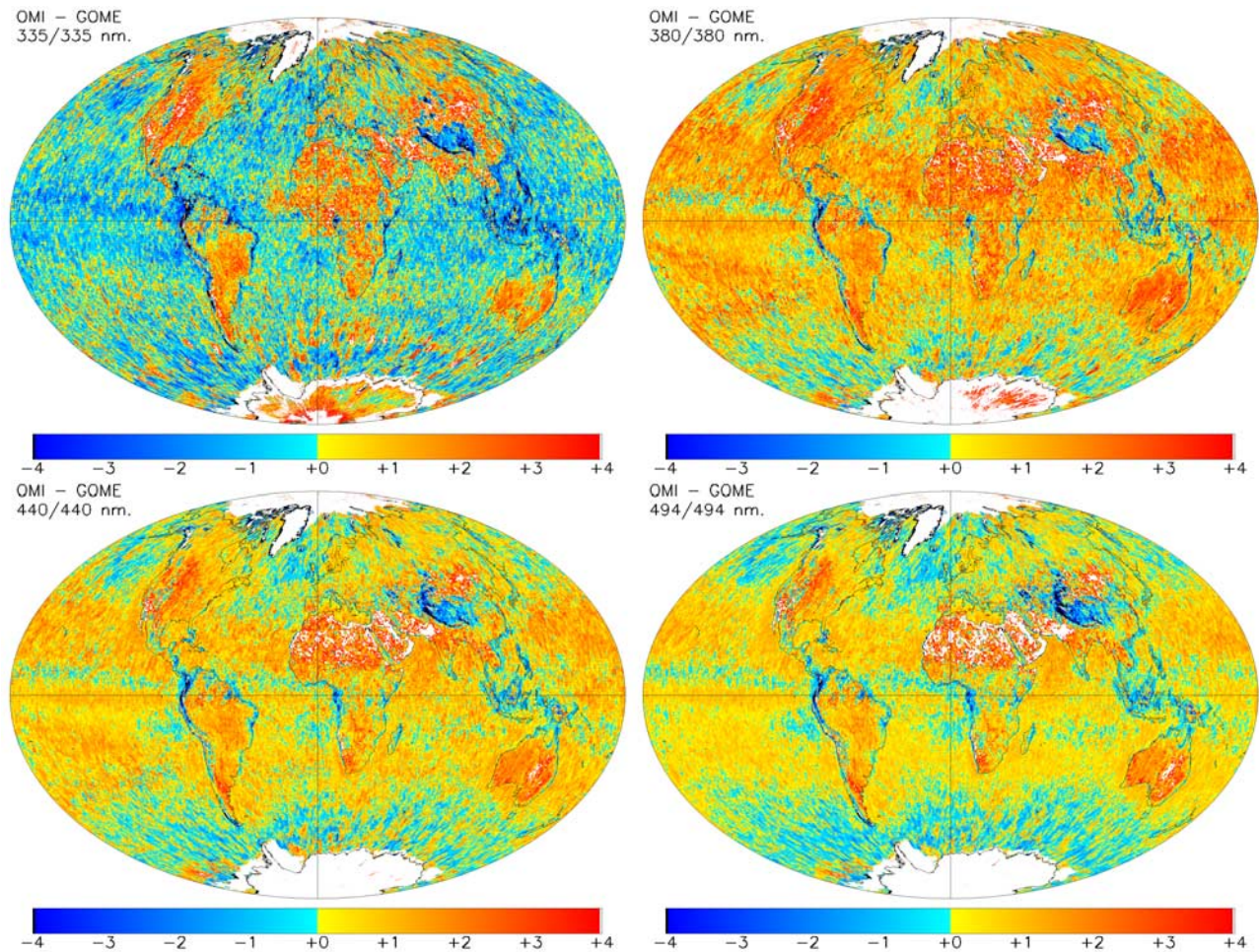


Figure 9. Difference in mission minimum LER between OMI and Global Ozone Monitoring Experiment (GOME). The values in the legend have been multiplied by 100.

470 nm for the entire globe and several regions of the Earth. Good agreement is found over bare land and deserts like the Sahara and central Australia and the permanent ice sheets; in these areas the OMI surface reflectances are approximately 0.01 higher than the MODIS black sky albedo values. This indicates that the BRDF model for these land types is consistent with the method used to derive the LER (mode of the histogram). Evidence of persistent cloud features in the OMI data are visible over the northern part of South America and the west coast of Africa. For all other land types the LER is 0.02 higher. This agreement is good considering the uncertainties and the different approaches used to derive these data sets.

6.2. Comparison With TOMS

[46] The mission minimum LER difference between OMI and TOMS/Nimbus 7 (as derived by *Herman and Celarier* [1997]) is given in Figure 8. The wavelengths used by TOMS are 331, 340, 360, and 380 nm. The corresponding wavelengths used by OMI are 328, 342, 354, and 380 nm, respectively. OMI surface reflectances can be up to 0.03 higher than TOMS MLER values with a significant north-south dependence. The average difference is 0.01 over the Northern Hemisphere and 0.02 over the Southern Hemisphere. This latitudinal effect becomes more pronounced at

shorter wavelengths and cannot easily be explained. Both polar ice caps are white in the graphs, showing that OMI surface reflectances are at least 0.04 higher than TOMS. The black patch over the Tibetan Plateau indicates that is equal or higher than OMI, which is unexpected, and may be related to the relatively low surface pressures in that area. It should be noted that the TOMS data set comprises 14.5 years, while OMI only contains 3 years of data; moreover, the time gap of 10 years between the two data sets could introduce unknown long-term seasonal effects. The equator crossing local time of Nimbus 7 is between 1030 LT (1993) and 1200 LT (1979). The elevated OMI surface reflectance over the northern part of South America and Sumatra are consistent with the aforementioned persistent cloud features.

6.3. Comparison With GOME

[47] We also compare the OMI LER to KHS03 data set (equator crossing time 1030 LT) data set. In Figure 9 the difference OMI-GOME is shown at 335, 380, 440, and 494 nm. The agreement at 494 nm over the Southern Hemisphere oceans is good, and there is no north-south dependence visible in contrast to the HC97 data set. *Koelmeijer* [2003] also noted this phenomenon but could not find an explanation; it is now more likely that this dependence is a feature of the HC97 data set. There is a significant difference

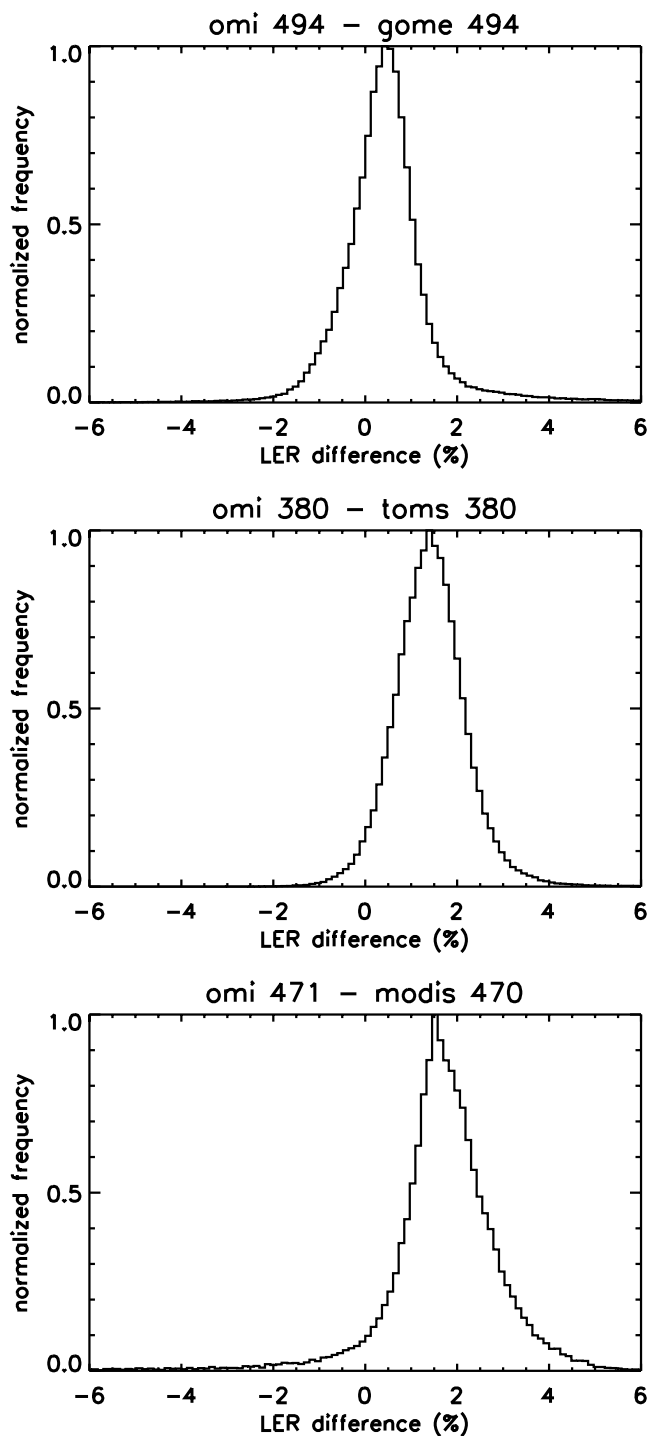


Figure 10. Distribution functions of the differences in minimum LER between OMI and GOME, TOMS, and MODIS, using only data between 60°S and 60°N.

between the values over water and over land for all UV wavelengths which was not evident in the HC97 set. The OMI surface reflectance over the polar ice sheets at 335 and 380 nm is in better agreement with GOME than with TOMS. In general, the surface reflectance derived from OMI is 0.02 higher than that KHS03.

[48] Histograms of the differences in minimum LER among OMI and GOME, TOMS, and MODIS, using only

data between 60°S and 60°N, are given in Figure 10 for three different wavelengths. The OMI surface reflectance is, on average, 0.006 higher than the GOME MLER data set at 494 nm, with a standard deviation of 0.014. The OMI surface reflectance at 380 nm is on average 0.015 higher than TOMS with a standard deviation of 0.012. The OMI surface reflectance is on average 0.018 higher than the MODIS black sky albedo with a standard deviation of 0.017. These higher values of the OMI data set are caused by the fact that we have chosen not to use the absolute minimum of the histogram but a slightly higher value as the representative value for the surface reflectance.

6.4. Comparison With the MLER

[49] In order to quantify the effect of using a statistical method instead of the absolute minimum value of the observations, we have calculated the difference between the OMI LER and the OMI MLER. The top image in Figure 11 gives the difference between the OMI LER and the MLER for a single month. Obviously the LER over bare lands and permanent ice and snow is higher than the MLER. Over the oceans the statistical approach only slightly differs with the MLER approach, except for regions known to be cloudy like the ITCZ. However, the difference over these regions is smaller than 0.01.

[50] We have also calculated the difference between the KHS03 data set that uses the MLER approach, and the OMI MLER. In Figure 11, the bottom image shows that KHS03 on average is higher than the OMI MLER, possibly indicating residual cloud contamination in the KHS03 data set. Especially the white patches over tropical rain forest indicate that KHS03 is more sensitive to cloud contamination, which in turn is most likely caused by the larger ground pixels.

7. OMI LER Mission Results

7.1. Mission LER at Various Wavelengths

[51] The minimum mission LER is shown in Figure 12, for four wavelengths. At 328 nm and 380 nm, the LER over land (0.00–0.02) is lower than over the sea (0.03–0.08), but both land and water have features outside this range. The highest LER values at this wavelength occur over North Africa and over areas of the Pacific Ocean. The reflective properties of coastal waters are, to a large extent, caused by reflective silt in the outflow of rivers. In open oceans, the pigments in phytoplankton absorb radiation at different wavelengths, depending on the specific type of pigment. High concentrations of phytoplankton, leading to low surface reflectance, occur in ocean regions with high algae content, often associated with upwelling of cold, nutrition rich, water. Examples of upwelling regions clearly visible in Figure 12 are those regions off the coasts of West Africa (Southern Hemisphere) and South America, and the narrow equatorial upwelling regions, in particular in the Pacific Ocean. All these features are also observed in HC97 and KHS03. The highest LER values over water occur at 380 nm with reflectances exceeding 0.10; the LER over land is usually in the range 0.03–0.09 and over the sea 0.05–0.09, with some higher values over deserts and certain areas in the Pacific. At 425 nm the oceans are brighter than land because the absorption by phytoplankton and yellow substance is

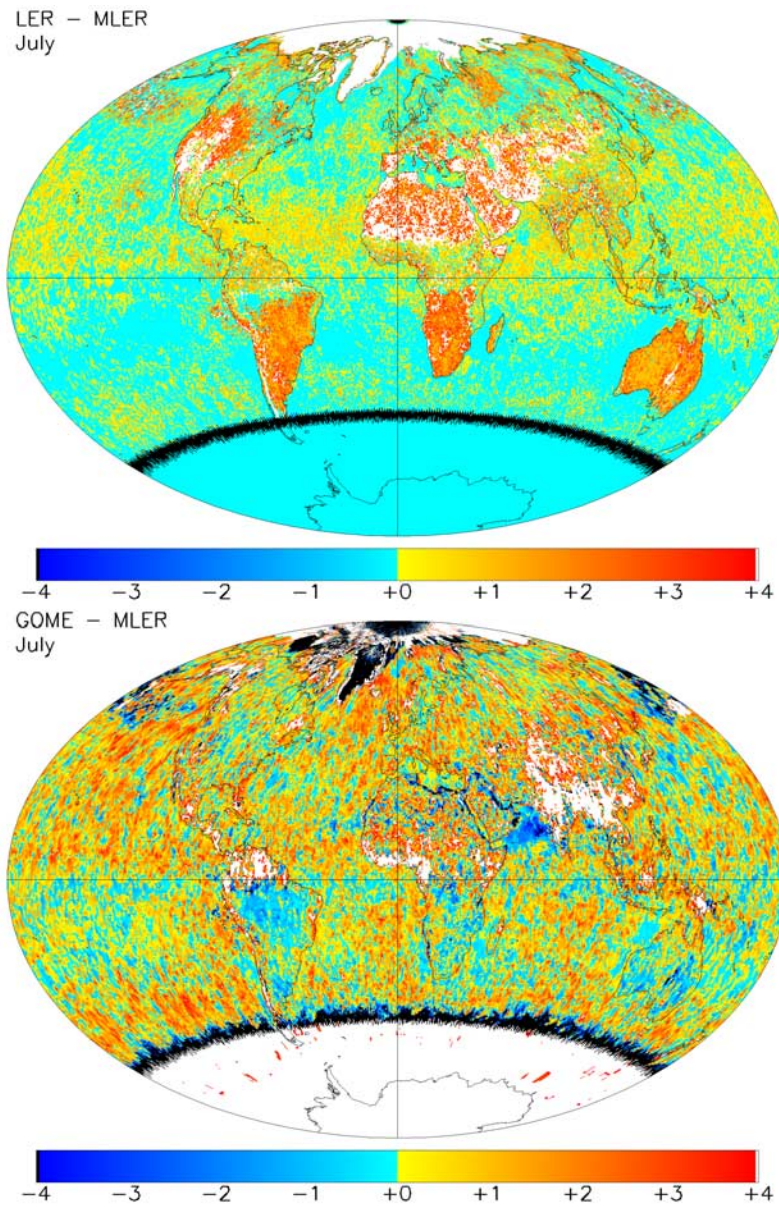


Figure 11. (top) Difference between the OMI LER based on a statistical approach, and the OMI minimum Lambertian equivalent reflectance (MLER). (bottom) The difference between the KHS03 MLER and the OMI MLER.

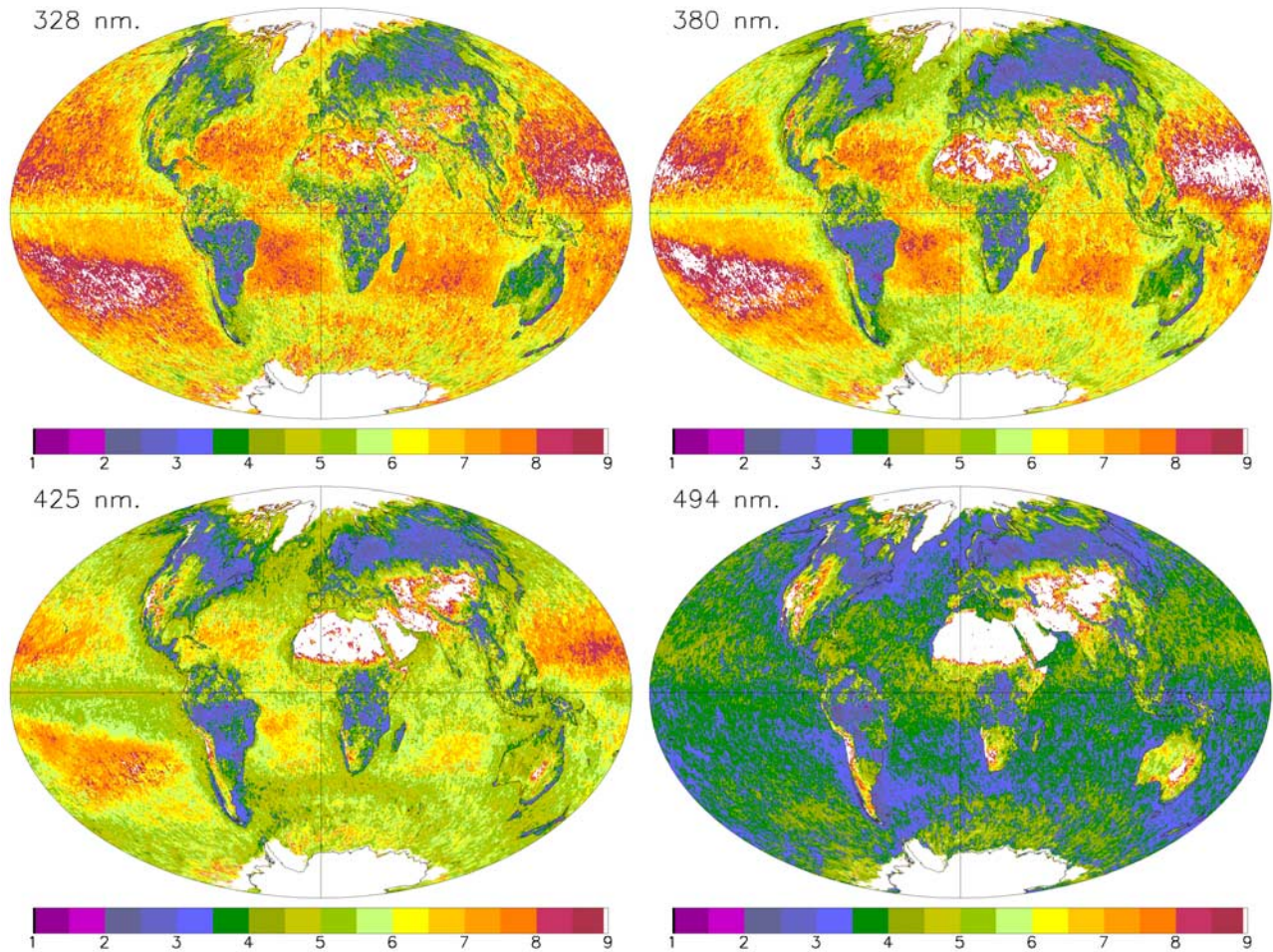


Figure 12. Minimum mission LER at four wavelengths. The values in the legend have been multiplied by 100. All values higher than the maximum value of the legend are colored white in order to enhance the details at the lower values.

less than at shorter wavelengths. At 494 nm the dominant absorber is water, leading to low LER values over sea and high values over land. LER values over sea also tend to be more homogeneous with values of 0.03–0.04; the remaining patches are caused by residual cloud contamination which introduces reflectances up to 0.05. The highest LER values over land occur over deserts at 494 nm where the reflectance can be as high as 0.30.

7.2. LER Seasonal Effects

[52] Figure 13 shows the seasonal effects in LER at 494 nm by subtracting the mission minimum from the monthly data sets. Because the mission map is the absolute minimum value no negative values occur in the plots. If the difference exceeds 0.02 the pixel is colored white, this mostly occurs in the case of snow and sea ice. High seasonal variations, that cannot be attributed to snow and ice effects, can be seen over the southern part of the Sahara in January, over India and south Australia in April, over parts of Northern America, South and northwest Africa and the Middle East in July, and over north Australia and Madagascar in October. The LER seasonal variation over the ocean is generally smaller than 0.012, with pronounced features in the South Pacific Ocean. Here the LER is at its

lowest in July and increases with 0.02 in October. This is in agreement with results from HC97 and KHS03. Figure 14 shows, on a monthly base, the seasonal variation of four selected areas over the Earth. The values plotted are the mean values over the Libyan desert (24°N, 19°E to 28°N, 26°E), the South Pacific Ocean (30°S, 120°W to 10°S, 100°W), South Angola (16°S, 12°E to 12°S, 21°E), and the North Atlantic Ocean (42°N, 45°W to 56°N, 17°W).

7.3. Spectral Properties of the LER

[53] The spectral dependency of the LER is categorized per surface type using a classification by *De Fries et al.* [1998]. Figure 15 shows the average spectrum over all ground pixels for the months January, April, July, and October. The data are taken from the combined mission map, using only data between 60°S and 60°N. A small feature at 477 nm is independent of the ground type and is caused by the O₂-O₂ absorption band which is not accounted for in the atmospheric correction applied. The reflectance of water below 390 nm is nearly wavelength independent. This is consistent with HC97, but not with KHS03, which also shows a flat spectrum but which sharply increases at 335 nm. The spectral dependence of broadleaf and needleleaf forests is consistent with KHS03, however

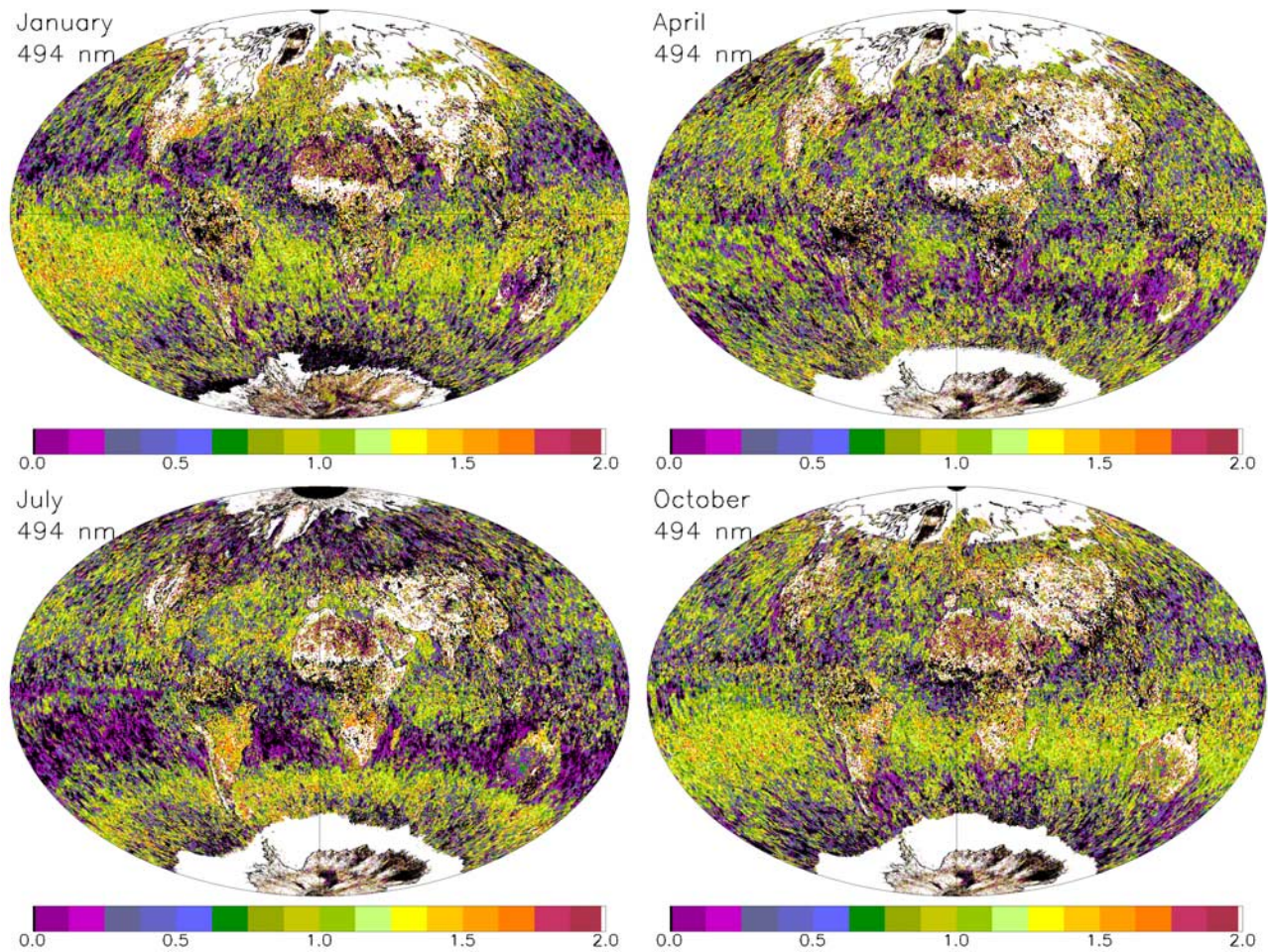


Figure 13. Seasonal effects in the LER at 494 nm. The values are obtained by subtracting the mission minimum from the monthly values. Because the mission value is the absolute minimum value, no negative values occur in the graphs. The numbers in the legend have been multiplied by 100. All values larger than 2% are plotted in white. Black indicates that the monthly value is equal to the mission minimum and hence occurred in that month.

grasses behave differently. The OMI surface reflectance for grasses drops with longer wavelengths whereas KHS03 indicates that it is increasing. This may be explained by the different land cover database used. The seasonal spectral dependence is also shown and does not vary much with land cover, with the exception of needleleaf forest.

[54] The spectral contrast between two wavelengths is shown in Figure 16 for two wavelength combinations (335–380 nm and 380–494 nm); the data are taken from the combined mission LER. The UV contrast generally has small negative values over the oceans with higher values over the phytoplankton rich waters in the Pacific; small positive values are only seen over the northern Atlantic Ocean with values up to 0.005. Over land the UV spectral contrast is generally low. Only over certain bare lands in North Africa and the Arabian Peninsula strong negative contrast exist with values exceeding -0.02 .

[55] The VIS spectral contrast between 380 nm and 494 nm shows more variability per land type than the UV contrast. The oceans can all be distinguished from land with positive values up to $+0.06$. The VIS contrast for forest areas is low, consistent with the observed spectral behavior

shown in Figure 15. Similar to the UV contrast, the phytoplankton rich waters stand out, but the VIS contrast is positive. The contrast over bare land areas is also negative for the VIS, especially for the deserts in North Africa, Arabia, Australia, and Mongolia.

[56] The black patches over bare lands in North Africa and the Arabian Peninsula are commonly associated with absorbing aerosols. However, these patches are evident in both the ultraviolet and the visible spectral contrast. This can be understood from the spectral reflectance of the land type as given in Figure 15. The reflectance of bare lands always increases toward the longer wavelengths and therefore the spectral contrast will be negative per definition. As long as the absorbing aerosol index is calculated under the assumption that the surface reflectance is equal at the two wavelengths the resulting AAI will depend on the land type. This is undesirable, and an improvement can be made by including the spectral surface reflectance in the calculation of the AAI. The black patches are thus predominantly caused by the color of the surface and not by aerosols due to biomass burning or desert storms.

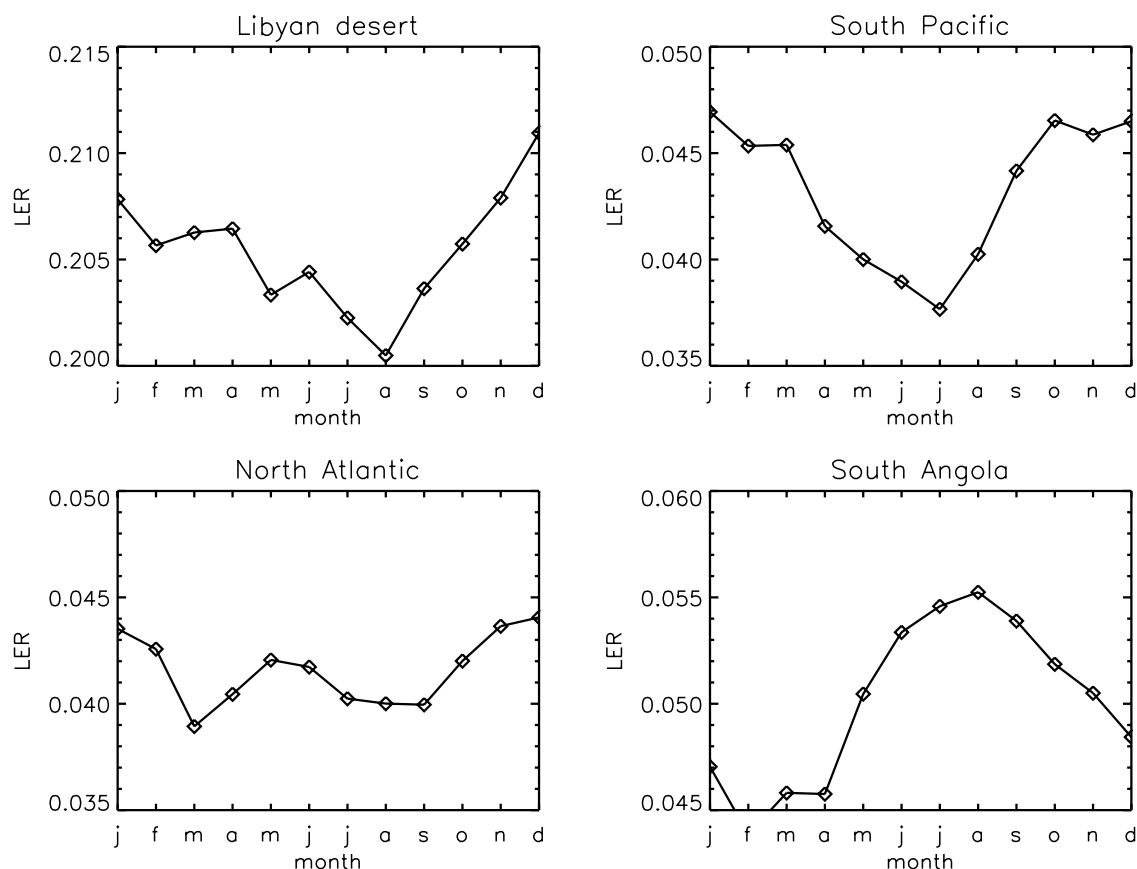


Figure 14. Seasonal dependence at 494 nm over selected areas: Libyan desert (24°N , 19°E to 28°N , 26°E), South Pacific Ocean (30°S , 120°W to 10°S , 100°W), South Angola (16°S , 12°E to 12°S , 21°E), and North Atlantic Ocean (42°N , 45°W to 56°N , 17°W).

[57] The yellow patches in the visible contrast over land indicate that the contrast is zero or slightly positive. These patches mainly correlate with broadleaf forests, however this behavior is not expected on the basis of the spectral dependence in Figure 15. It is expected that the ultraviolet spectral contrast is negative in case of biomass burning. However, broadleaf forest always have a positive contrast. The patches also correlate with the persistent cloud features over Brazil, central Africa, China, and Southeast Asia, as can be seen in Figure 2. The fact that the visible contrast is close to zero indicates cloud contamination which will affect the calculation of the absorbing aerosol index. For this reason, future mission will benefit from smaller ground pixel sizes.

8. Conclusion and Outlook

[58] Using 3 years of OMI data we have derived a global climatology of the Earth's surface Lambertian equivalent reflectance with a temporal resolution of one month and a spatial resolution of 0.5° by 0.5° in the wavelength range 328 to 500 nm. The data set is an extension and continuation of similar existent data sets created from TOMS and GOME data, all aimed at supporting and improving retrievals of concentrations of atmospheric trace gases and properties of clouds and aerosols from UV/VIS satellite spectrometers. The OMI data set contains more wave-

lengths, especially in the ultraviolet region, and has a higher spatial resolution, allowing more precise retrievals for trace gases in the wavelength range of 328–500 nm. Special attention has been given to the shorter UV wavelengths by including a first-order guess of the total ozone column. The ultraviolet global surface reflectances are less accurate than the VIS LER values, mainly because of increasing ozone absorption toward the shorter wavelengths. The data set is distributed as a single file in the Hierarchical Data Format (HDF5) and can be obtained at the OMI project website at the KNMI (<http://www.knmi.nl/omi>), as well as through the Goddard Earth Sciences Data and Information Services Center (<http://disc.sci.gsfc.nasa.gov/>).

[59] The OMI scene reflectance data set is derived using a different approach than its precursors in order to yield an climatologically averaged reflectance that includes the presence of ground haze and persistent cloud features. This leads to an higher value of the surface reflectance than one based on an absolute minimum method. Compared to the TOMS and GOME based data sets, the OMI LER is approximately 0.015 and 0.006 higher, respectively, with standard deviations of 0.012 and 0.014, respectively. Evidence is presented for a small north-south bias in the TOMS data set, which is not present in the GOME and OMI data sets. The consistency with MODIS data is satisfactory considering that both products are related but do not describe the same surface property. The overall accuracy

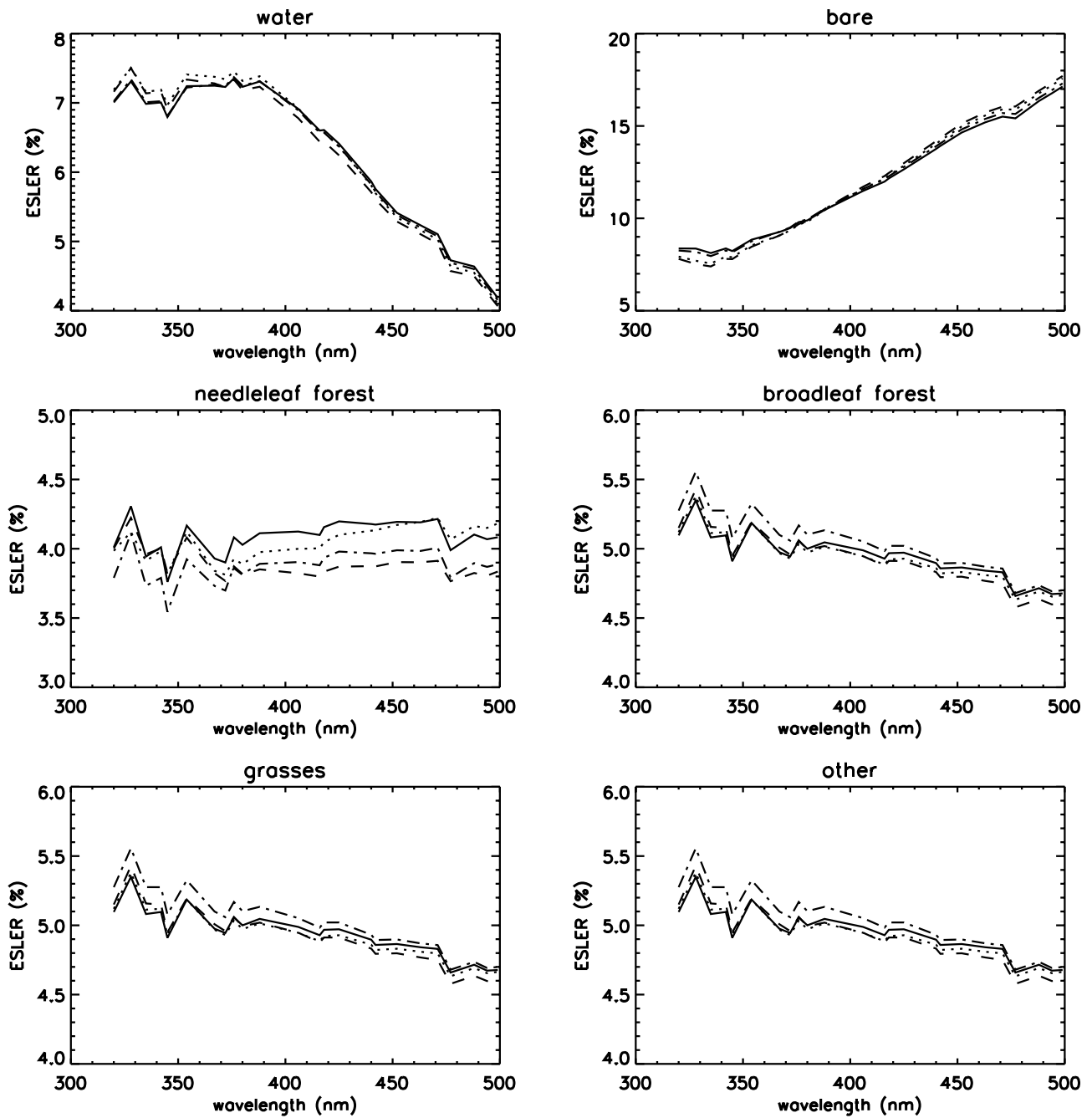


Figure 15. Spectral dependence of the LER for different land types according to the classification by *De Fries et al.* [1998]. The data are taken from the combined mission map, using only data between 60°S and 60°N. The mean value over all ground pixels is given for January (solid line), April (dotted line), July (dashed line), and October (dash-dotted line).

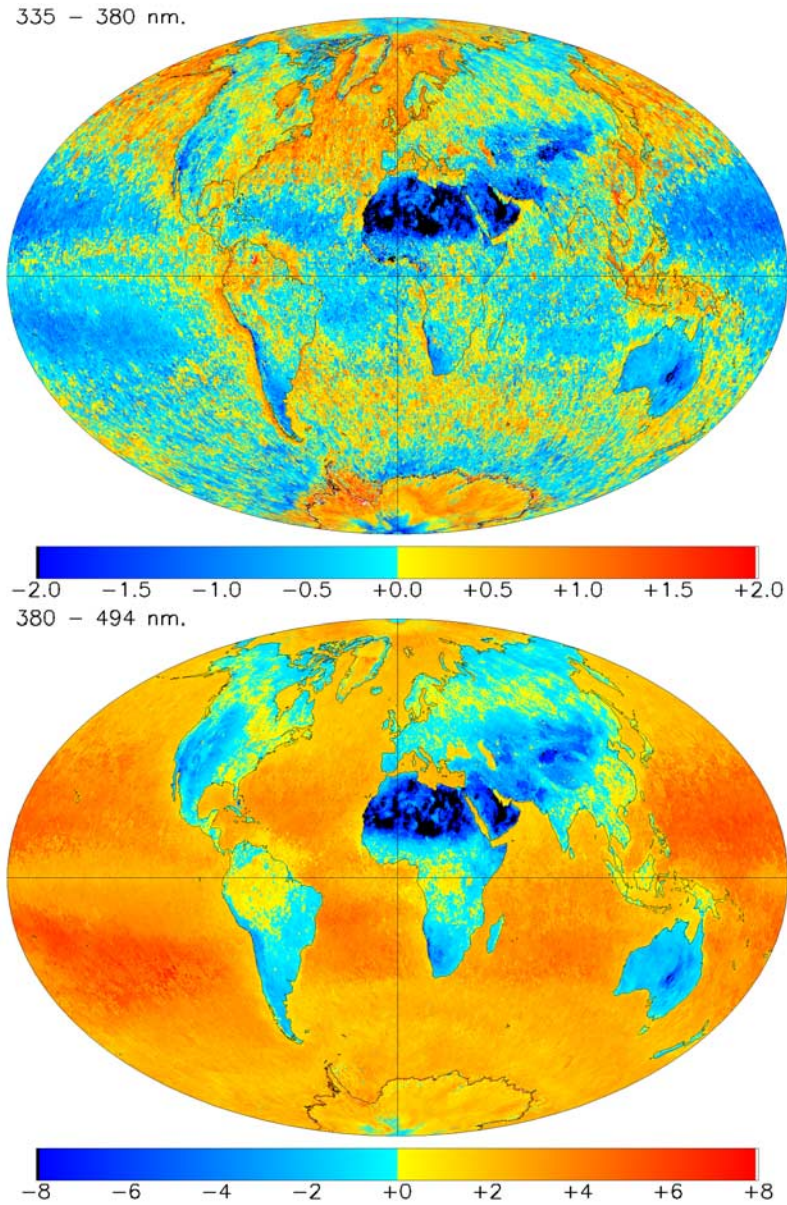


Figure 16. Difference of the spectral minimum mission LER at two wavelengths multiplied by 100. The top image shows the 335–380 difference, while the bottom image shows the 380–494 difference, both in absolute LER percentiles. The black patches over North Africa are regions where the difference exceeds 0.02 and 0.08, respectively.

of the OMI LER climatology is approximately 0.01 to 0.02 for the longer wavelengths and increasing toward the shorter ultraviolet wavelengths. It is shown that the spectral behavior of the surface reflectance strongly depends on land type. Therefore, the ultraviolet spectral contrast depends on land type, and this should be included in the calculation of the aerosol absorbing index, especially over bare land types. Cloud contamination is a significant source of error for the calculation of the surface reflectance, and all products that depend on it, and can be reduced by using smaller ground pixels in future missions.

[60] Future work will focus on the improvement of the presented data set, by including more data when these become available, in order to further reduce the residual cloud contamination over tropical regions. Using measured total ozone column data in the atmospheric correction will improve the accuracy of the data set at shorter UV wavelengths. When sufficient data are available, it will become feasible to characterize the viewing angle dependence of the scene's reflectivity as seen by OMI.

[61] **Acknowledgments.** The authors would like to thank P. Stammes and G. Jaross for assistance during the initial stage of this project. We thank P. Veeffkind for general discussions and the verification of the product, as well as N. Rozemeijer and the TMCF team for assistance with the data processing. We also wish to thank three anonymous reviewers for their valuable comments. This work was performed with financial support from the National Agency for Aerospace Programmes of The Netherlands (NIVR).

References

- Asner, G. P. (2001), Cloud cover in Landsat observations of the Brazilian Amazon, *Int. J. Remote Sens.*, *22*(18), 3855–3862, doi:10.1080/01431160010006926.
- Boersma, K. F., H. J. Eskes, and E. J. Brinksma (2004), Error analysis for tropospheric NO₂ retrieval from space, *J. Geophys. Res.*, *109*, D04311, doi:10.1029/2003JD003962.
- Brion, J., A. Chakir, D. Daumont, and J. Malicet (1993), High-resolution laboratory absorption cross section of O₃: Temperature effect, *Chem. Phys. Lett.*, *213*(5–6), 610–612, doi:10.1016/0009-2614(93)89169-1.
- Brion, J., A. Chakir, J. Charbonnier, D. Daumont, C. Parisse, and J. Malicet (1998), Absorption spectra measurements for the ozone molecule in the 350–830 nm region, *J. Atmos. Chem.*, *30*, 291–299, doi:10.1023/A:1006036924364.
- Bucselo, E. J., et al. (2006), Algorithm for NO₂ vertical column retrieval from the Ozone Monitoring Instrument (OMI) using the DOAS technique, *IEEE Trans. Geosci. Remote Sens.*, *44*(5), 1245–1258.
- Csiszar, I., and G. Gutman (1999), Mapping global land surface albedo from NOAA AVHRR, *J. Geophys. Res.*, *104*(D6), 6215–6228.
- Daumont, M., J. Brion, J. Charbonnier, and J. Malicet (1992), Ozone UV spectroscopy, I: Absorption cross-sections at room temperature, *J. Atmos. Chem.*, *15*, 145–155, doi:10.1007/BF00053756.
- De Fries, R. S., M. Hansen, J. R. G. Townshend, and R. Sohlberg (1998), Global land cover classifications at 8 km spatial resolution: The use of training data derived from Landsat imagery in decision tree classifiers, *Int. J. Remote Sens.*, *19*(16), 3141–3168, doi:10.1080/014311698214235.
- De Haan, J. F., P. B. Bosma, and J. W. Hovenier (1987), The adding method for multiple scattering calculations of polarized light, *Astron. Astrophys.*, *183*, 271–391.
- Diner, D. J., J. C. Beckert, G. W. Bothwell, and J. I. Rodriguez (2002), Performance of the MISR instrument during its first 20 months in Earth orbit, *IEEE Trans. Geosci. Remote Sens.*, *40*(7), 1449–1466, doi:10.1109/TGRS.2002.801584.
- Dirksen, R., M. Dobber, R. Voors, and P. Levelt (2006), Prelaunch characterization of the Ozone Monitoring Instrument transfer function in the spectral domain, *Appl. Opt.*, *45*(17), doi:10.1364/AO.45.003972.
- Dobber, M. R., et al. (2006), Ozone Monitoring Instrument calibration, *IEEE Trans. Geosci. Remote Sens.*, *44*(5), 1209–1238.
- Dobber, M., Q. L. Kleipool, R. Dirksen, P. Levelt, G. Jaross, S. Taylor, T. Kelly, L. Flynn, G. Leppelmeier, and N. Rozemeijer (2008a), Validation of Ozone Monitoring Instrument level 1b data products, *J. Geophys. Res.*, *113*, D15S06, doi:10.1029/2007JD008665.
- Dobber, M., R. Voors, R. Dirksen, and Q. L. Kleipool (2008b), The high-resolution solar reference spectrum between 250 and 550 nm and its application to measurements with the Ozone Monitoring Instrument, *Sol. Phys.*, *249*, 281–291, doi:10.1007/s11207-008-9187-7.
- Herman, J. R., and E. A. Celarier (1997), Earth surface reflectivity climatology at 340–380 nm from TOMS data, *J. Geophys. Res.*, *102*(D23), 28,003–28,011.
- Herman, J. R., E. Celarier, and D. Larko (2001), UV 380 nm reflectivity of the Earth surface, clouds and aerosols, *J. Geophys. Res.*, *106*(D6), 5335–5351.
- Jaross, G., and J. Warner (2008), Use of Antarctica for validating reflected solar radiation measured by satellite sensors, *J. Geophys. Res.*, *113*, D16S34, doi:10.1029/2007JD008835.
- Joiner, J., and A. P. Vasilkov (2006), First results from the OMI rotational Raman scattering cloud pressure algorithm, *IEEE Trans. Geosci. Remote Sens.*, *44*(5), 1272–1282.
- Koelemeijer, R. B. A., P. Stammes, J. W. Hovenier, and J. F. de Haan (2001), A fast method for retrieval of cloud parameters using oxygen a band measurements from the Global Ozone Monitoring Experiment, *J. Geophys. Res.*, *106*(D4), 3475–3490.
- Koelemeijer, R. B. A., J. F. de Haan, and P. Stammes (2003), A database of spectral surface reflectivity in the range 335–772 nm derived from 5.5 years of GOME observations, *J. Geophys. Res.*, *108*(D2), 4070, doi:10.1029/2002JD002429.
- Krijger, J. M., M. van Weele, I. Aben, and R. Frey (2007), The effect of sensor resolution on the number of cloud-free observations from space, *Atmos. Chem. Phys.*, *7*, 2881–2891.
- Krotkov, N. A., S. A. Carn, A. J. Kreuger, P. K. Bhartia, and K. Yang (2006), Band residual difference algorithm for retrieval of SO₂ from the AURA Ozone Monitoring Instrument (OMI), *IEEE Trans. Geosci. Remote Sens.*, *44*(5), 1259–1266.
- Leppelmeier, G. W., O. Aulamo, S. Hassinen, A. Malkki, T. Riihisaari, R. Tajakka, J. Tamminen, and A. Tanskanen (2006), OMI very fast delivery and the Sodankyla satellite data centre, *IEEE Trans. Geosci. Remote Sens.*, *44*(5), 1283–1287.
- Le Treut, H., R. Somerville, U. Cubasch, Y. Ding, C. Mauritzen, A. Mokssit, T. Peterson, and M. Prather (2007), Historical overview of climate change, in *Climate Change 2007: The Physical Science Basis. Contribution of Working Group I to the Fourth Assessment Report of the Intergovernmental Panel on Climate Change*, edited by S. Solomon et al., Cambridge Univ. Press, New York.
- Levelt, P. F., G. H. J. van den Oord, M. R. Dobber, A. Malkki, H. Visser, J. de Vries, P. Stammes, J. O. V. Lundell, and H. Saari (2006a), The Ozone Monitoring Instrument, *IEEE Trans. Geosci. Remote Sens.*, *44*(5), 1093–1101.
- Levelt, P. F., E. Hilsenrath, G. W. Leppelmeier, G. H. J. van den Oord, P. K. Bhartia, J. Tamminen, J. F. de Haan, and J. P. Veeffkind (2006b), Science objectives of the Ozone Monitoring Instrument, *IEEE Trans. Geosci. Remote Sens.*, *44*(5), 1199–1209.
- Levy, R. C., L. A. Remer, S. Mattoo, E. F. Vermote, and Y. J. Kaufman (2007), Second-generation operational algorithm: Retrieval of aerosol properties over land from inversion of Moderate Resolution Imaging Spectroradiometer spectral reflectance, *J. Geophys. Res.*, *112*, D13211, doi:10.1029/2006JD007811.
- Malicet, C., D. Daumont, J. Charbonnier, C. Parisse, A. Chakir, and J. Brion (1995), Ozone UV spectroscopy, II: Absorption cross-sections and temperature dependence, *J. Atmos. Chem.*, *21*, 263–273, doi:10.1007/BF00696758.
- Martin, R. V., et al. (2002), An improved retrieval of tropospheric nitrogen dioxide from GOME, *J. Geophys. Res.*, *107*(D20), 4437, doi:10.1029/2001JD001027.
- Moody, E. G., M. D. King, S. Platnick, C. B. Schaaf, and F. Gao (2005), Spatially complete global spectral surface albedos: Value-added datasets derived from Terra MODIS land products, *IEEE Trans. Geosci. Remote Sens.*, *43*, 144–158, doi:10.1109/TGRS.2004.838359.
- Nolin, A., R. L. Armstrong, and J. Maslanik (1998), Near real-time SSM/I EASE-Grid daily global ice concentration and snow extent, 2004 to 2008, <http://nsidc.org/data/nise1.html>, Natl. Snow and Ice Data Cent., Boulder, Colo.
- Oord, G. H., et al. (2006), OMI level 0 to 1b processing and operational aspects, *IEEE Trans. Geosci. Remote Sens.*, *44*(5), 1380–1397.
- Schaaf, C. B., et al. (2002), First operational BRDF, albedo nadir reflectance products from MODIS, *Remote Sens. Environ.*, *83*, 135–148, doi:10.1016/S0034-4257(02)00091-3.
- Schoeberl, M. R., et al. (2006), Overview of the EOS Aura Mission, *IEEE Trans. Geosci. Remote Sens.*, *44*(5), 1066–1074.
- Stammes, P. (2001), Spectral radiance modeling in the UV-visible range, in *Proceedings URS-2000: Current Problems in Atmospheric Radiation*, edited by W. L. Smith and Y. N. Timofeyev, pp. 385–388, A. Deepak, Hampton, Va.

- Tanskanen, A., N. A. Krotkov, J. R. Herman, and A. Arola (2006), Surface ultraviolet irradiance from OMI, *IEEE Trans. Geosci. Remote Sens.*, *44*(5), 1267–1271.
- van de Hulst, H. C. (1980), *Multiple Light Scattering: Tables, Formulas, and Applications*, vol. 1, Elsevier, New York.
- Veefkind, J. P., G. de Leeuw, P. Stammes, and R. B. A. Koelemeijer (2000), Remote distribution of aerosol over land, derived from ATSR-2 and GOME, *Remote Sens. Environ.*, *74*(3), 377–386.
- Veefkind, J. P., J. de Haan, E. J. Brinksma, M. Kroon, and P. F. Levelt (2006), Total ozone from the Ozone Monitoring Instrument (OMI) using the DOAS technique, *IEEE Trans. Geosci. Remote Sens.*, *44*(5), 1239–1244.
- Voors, R., M. Dobber, R. Dirksen, and P. Levelt (2006), Method of calibration to correct for cloud-induced wavelength shifts in the Aura satellite's Ozone Monitoring Instrument, *Appl. Opt.*, *45*(15), 3652–3658, doi:10.1364/AO.45.003652.
- Wylie, D., D. L. Jackson, W. P. Menzel, and J. J. Bates (2005), Trends in global cloud cover in two decades of HIRS observations, *J. Clim.*, *18*, 3021–3031, doi:10.1175/JCLI3461.1.

J. F. de Haan, M. R. Dobber, Q. L. Kleipool, and P. F. Levelt, Royal Netherlands Meteorological Institute, P.O. Box 201, NL-3730 AE, De Bilt, Netherlands. (kleipool@knmi.nl)